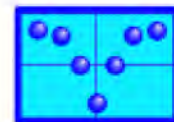
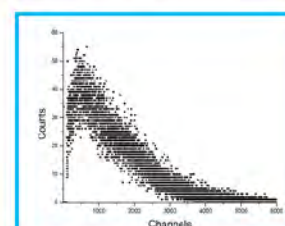
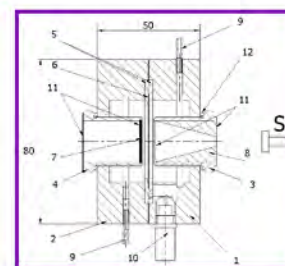
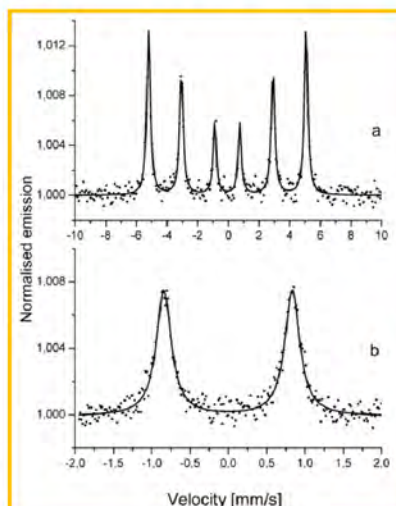
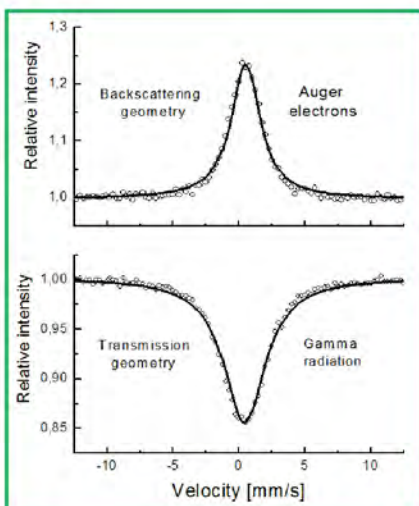
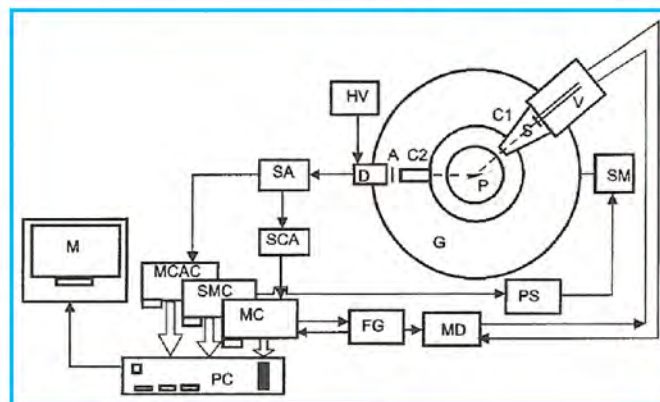
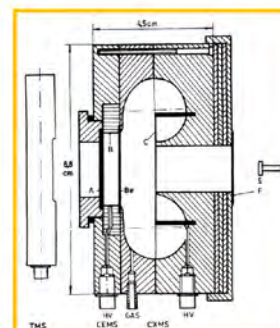


# Mössbauer Effect Reference and Data Journal

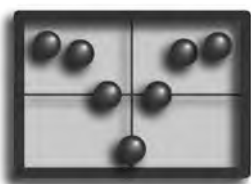


May • Volume 47 • Number 03

**Ph.D. Dipl. Eng. ION BIBICU**  
**More Than 45 Years Worked in Mössbauer Spectroscopy**



# Mössbauer Effect Reference and Data Journal



## Editors

Tao Zhang  
*Director*

Frank Berry, John Stevens  
*Honorary Directors*

Junhu Wang  
*Secretary General*

Alexandre Rykov, Rile Ge  
*Research Associates*

Duorong (Lucy) Liu  
*Editorial Assistants*

## Associate Editors

BELGIUM  
Y. Garcia

CHINA  
J. F. Li

COLOMBIA  
C. A. Barrero

CZECH  
L. Machala

FRANCE  
M.T. Sougrati

HUNGARY  
K. Lázár  
Z. Klencsár

JAPAN  
S. Kubuki  
S. Tsutsui

KOREA  
C. S. Kim

POLAND  
S. M. Dubiel

RUSSIA  
M. I. Oshtrakh  
V. G. Semenov

USA  
E. E. Alp  
R. P. Hermann

## MEDC International Advisory Board

AUSTRALIA  
S. J. Campbell – *University of New South Wales*

AUSTRIA  
M. Reissner – *Technische Universität Wien*

BELGIUM  
Y. Garcia – *Université Catholique de Louvain*

BRAZIL  
J. D. Fabris – *Universidade Federal de Minas Gerais*

CHINA  
J. Y. Shen – *Nanjing University*

CZECH  
L. Machala – *Palacký University in Olomouc*

FRANCE  
J. M. Grenèche – *Université de Maine*  
R. Rüffer – *European Synchrotron Radiation Facility*

GERMANY  
F. Renz – *Leibniz Universität Hannover*  
H. Engelmann – *WissEl - Wissenschaftliche Elektronik GmbH*

HUNGARY  
E. Kuzmann – *Eötvös Loránd University*  
K. Lázár – *Centre for Energy Research*  
Z. Klencsár – *Centre for Energy Research*

JAPAN  
M. Takahashi – *Toho University*  
S. Kubuki – *Tokyo Metropolitan University*

KOREA  
C. S. Kim – *Kookmin University*

RUSSIA  
M. I. Oshtrakh – *Ural Federal University*

SPAIN  
J. F. Marco – *Instituto de Química-Física "Rocasolano"*

USA  
R. P. Hermann – *Oak Ridge National Laboratory*

The *Mössbauer Effect Reference and Data Journal (MERDJ)* is published ten times a year (each month excluding January and February) plus an Index Issue at the end of December by the Mössbauer Effect Data Center.

Subscriptions: The annual subscription rate for Volume 47 (2024) is US\$1,500.00 (\$1,200.00 without the Index Issue). Subscription inquiries and address changes should be addressed to the General Manager at the address below.

Mössbauer Effect Data Center  
Dalian Institute of Chemical Physics  
Chinese Academy of Sciences  
457 Zhongshan Road, Dalian  
116023, China

Tel: +86 411 8437 9407  
Email: [medc@dicp.ac.cn](mailto:medc@dicp.ac.cn)  
Web: [www.medc.dicp.ac.cn](http://www.medc.dicp.ac.cn)

ISSN 0163-9587

### On the cover:

This special issue our front cover is focusing on Ph.D. Dipl. Eng. ION BIBICU, a full membership holder of the Technical Sciences Academy of Romania. We're lucky we can enjoy his over 45 years' Mössbauer research stories (See more in Editor's Comments and in the enclosed Mössbauer Spectroscopy Newsletter.)

## Contents

Contents.....	69
Reference Listing .....	71
Data Listing .....	76
Subject Index .....	85
Abbreviation Listing .....	86
Isotope Index.....	86
Mössbauer Newsletter.....	87

---

## Editor's Comments

### More Than 45 Years Worked in Mössbauer Spectroscopy

Ph.D. Dipl. Eng. ION BIBICU, a full membership holder of the Technical Sciences Academy of Romania, has more than 45 years' Mössbauer spectroscopy research experience. He wrote this review from four directions: a) permanently ensuring the proper functioning of the installations; b) supporting an economic activity, complementary to the scientific activity of the collective; c) possibilities to extend and improve Mössbauer measurements; d) defining a personal research direction.

It's our pleasure to read Ph.D. Dipl. Eng. ION BIBICU's review on his Mössbauer research experience. He published many papers in the field of Mössbauer Spectroscopy. He thinks his below two papers are the most successful and worth recommending:

1. I. Bibicu, *Some comments on  $^{151}\text{Eu}$  Surface Mössbauer Spectroscopy*, Eur. Phys. J. Appl. Phys., 62 (1) (2013) 11302 (3 pages) DOI: <http://dx.doi.org/10.1051/epjap/2013120328>
2. I. Bibicu, G. Nicolescu, C. Cretu, *A versatile gas-flow proportional counter for Mössbauer spectroscopy*, Hyperfine Interactions 192 (1) (2009) 85-91; DOI: 10.1007/s10751-009-9950-7

We'd like to express our sincerely thanks to Ph.D. Dipl. Eng. ION BIBICU for his great contribution to our Mössbauer Community. And we also hope he can have a wonderful retired life.

Junhu Wang  
Secretary General  
Executive Editor-in-Chief



## *Mössbauer Effect Data Center*

*is pleased to offer these publications and services to the international Mössbauer community...*

Mössbauer Effect  
Reference and Data Journal



It's all about the battery ...

## Mössbauer Effect Reference and Data Journal



The *Journal* reports as thoroughly as possible all published information on Mössbauer spectroscopy. An annual subscription includes ten issues plus an index issue. Each issue includes a Reference Listing, a Data Listing, an Isotope Index, a Subject Index, and the *Mössbauer Spectroscopy Newsletter*.

## Mössbauer Web Sites ON THE WORLD WIDE WEB



The Mössbauer Effect Data Center developed and administers two separate Web sites for the Mössbauer community

(<[www.moss.dicp.ac.cn](http://www.moss.dicp.ac.cn)> and <[www.medc.dicp.ac.cn](http://www.medc.dicp.ac.cn)>). These sites provide Mössbauer researchers with pertinent and timely information, free of charge. Included on the sites are general information pertinent to the Mössbauer community, news items, regional lab information, position postings, information on upcoming conferences, the most recent *Mössbauer Spectroscopy Newsletter*, IBAME information, an E-Mail and Fax Directory of Mössbauer Authors, links to Mössbauer instrument and source suppliers, and further information regarding the Center's products and services. Access to the MEDC Web-Access Database is also provided through the MEDC site. Researchers may now access and search the MEDC database *from their computers* via the MEDC Web site.

*For further information about these and our many other publications and services for the Mössbauer community, please visit us at our Web site*

Dalian Institute of Chemical Physics  
Chinese Academy of Sciences  
457 Zhongshan Road, Dalian 116023, China  
Phone: +86-411-84379159  
Fax: +86-411-84685940  
Email: [medc@dicp.ac.cn](mailto:medc@dicp.ac.cn)  
Web: [www.medc.dicp.ac.cn](http://www.medc.dicp.ac.cn) [www.moss.dicp.ac.cn](http://www.moss.dicp.ac.cn)

Code	Reference
22M052	H.Masenda, H.P.Gunnlaugsson, R.Adhikari, K.Bharuth-Ram, D.Naidoo, A.T.Martin-Luengo, I.Unzueta, R.Mantovan, T.E.Molholt, K.Johnston, J.Schell, A.M.Gerami, P.B.Krastev, B.C.Qi, S.Ólafsson, H.P.Gislason, A.Ernst, and A.Bonanni, <i>New J. Phys.</i> <b>24</b> (10),103007(2022) Unusual charge states and lattice sites of Fe in $\text{Al}_x\text{Ga}_{1-x}\text{N}:\text{Mn}$ .
23H037	N.Heppe, C.Gallenkamp, R.Z.Snitkoff-Sol, S.D.Paul, N.S.Salas, D.C.Moritz, B.Kaiser, W.Jaegermann, V.Potapkin, A.Jafari, V.Schünemann, O.Leupold, L.Elbaz, V.Krewald, and U.I.Kramm*, <i>ChemRxiv</i> ,1-16(2023) Applying nuclear forward scattering as in situ and operando tool for the characterization of $\text{FeN}_4$ moieties in the hydrogen evolution reaction.
23M059	A.V.Marchenko, E.I.Terukov, F.S.Nasredinov, V.S.Kiselev, and P.P.Seregin*, <i>Tech. Phys. Lett.</i> <b>49</b> (S4), S334-7(2023) Investigation of sodium and copper halides by the method of Mössbauer spectroscopy on the isotope $^{67}\text{Zn}$ .
23O012	M.J.Oliva, G.A.Pasquevich*, and A.L.Veiga*, <i>Hyperfine Interact.</i> <b>244</b> (1),23(2023) Embedded device for digitalizing monitor and error signals in Mössbauer spectroscopy.
23S094	A.V.Sobolev, S.Sandalova, M.N.Smirnova, A.A.Belik, I.S.Glazkova*, and I.A.Presniakov, <i>Russ. J. Inorg. Chem.</i> <b>68</b> (10),1349-1356(2023) Structure of the local environment and hyperfine interactions of $^{57}\text{Fe}$ probe nuclei in $\text{AMnO}_3$ (A=Sc, In).
23S097	M.Sobota, K.Idczak, R.Konieczny, and R.Idczak*, <i>Coatings</i> <b>13</b> (10),1679(2023) Corrosion resistance of Fe-Cr-Si alloy powders prepared by mechanical alloying.
23Y024	G.Y.Yurkov, A.V.Kozinkin*, S.P.Kubrin, A.Zhukov, S.Podskukhina, V.G.Vlasenko, A.Fionov, V.Kolesov, D.Zvyagintsev, M.Vyatkina, and V.I.Solodilov, <i>Polymers (Basel, Switz.)</i> <b>15</b> (19),3988(2023) Nanocomposites based on polyethylene and nickel ferrite: preparation, characterization, and properties.
24A005	B.Abdelwahab, G.S.M.Ahmed*, M.El-Ghazaly, A.Zoulfakar, and S.M.Salem, <i>Ann. Nucl. Energy</i> <b>198</b> , 110292(2024) Mössbauer spectroscopy and gamma-ray shielding performance for iron phosphate glasses containing various heavy metals oxides.
24A006	A.O.Alekseev, and T.V.Alekseeva, <i>Eurasian Soil Sci.</i> <b>57</b> (1),63-73(2024) Mineralogy and magnetic properties of the loess-soil formation as the reflection of the landscape and climatic conditions in the Terek-Kuma lowland in the Pleistocene.
24A007	L.Amin, R.A.Al-Juboori, F.Lindroos, M.Bounouba, K.Blomberg, M.L.Viveros, M.Graan, S.Azimi, J.Linden, A.Mikola, and M.Sperandio, <i>Sci. Total Environ.</i> <b>912</b> ,169520(2024) Tracking the formation potential of vivianite within the treatment train of full-scale wastewater treatment plants.
24A008	M.Ansari, S.Bhattacharjee, and D.A.Pantazis*, <i>J. Am. Chem. Soc.</i> <b>146</b> (14),9640-56(2024) Correlating structure with spectroscopy in ascorbate peroxidase compound II.
24A009	M.R.Araujo, L.S.P.Maia, M.A.R.Miranda, Y.Martinez-Camejo, J.M.Sasaki, and G.F.Guimaraes, <i>Sens. Actuators, A</i> <b>366</b> ,114923(2024) Optimization of nanoparticles for application in optical sensors.
24A010	A.M.Abdallah, M.Rabaa, H.Basma, Z.Bitari, N.Yaacoub, R.Sayed Hassan, and R.Awad, <i>J. Mater. Sci.: Mater. Electron.</i> <b>35</b> (3),245(2024) Enhancement of the physico-mechanical properties of La-doped Mg-Ni-Co tri-ferrites.
24A011	Y.Amako, T.Shiozawa, M.Nakashima, H.Yako, T.Eto, Y.Adachi, and T.Kanomata, <i>J. Magn. Magn. Mater.</i> <b>590</b> , 171675(2024) Magnetic properties of the off-stoichiometric Heusler alloys $\text{Rh}_2\text{Mn}_{1+x}\text{Sn}_{1-x}$ .
24B010	F.Bzour, I.Z.Al-Yahmadi, A.M.Gismelssed*, F.Al Ma'Mari, O.Cespedes, A.D.Al-Rawas, and H.M.Widatallah, <i>Physica. Condensed matter.</i> <b>673</b> ,415507(2024) Crystal structure, magnetic and Mössbauer studies of $\text{DyFe}_x\text{Mn}_{1-x}\text{O}_3$ multiferroic manganites.
24B011	A.Banerjee, A.Das, A.Saha, D.Das, and S.Sarkar, <i>J. Alloys Compd.</i> <b>970</b> ,172456(2024) Magnetic orderings in $\text{BaTi}_{1-x}\text{Fe}_x\text{O}_{3-\delta}$ (with $x=0.1$ ).
24B012	K.A.Béres, Z.Homonnay, and L.Kótai*, <i>ACS OMEGA</i> <b>9</b> (10),11148-67(2024) Hexakis(urea-O)iron complex salts as a versatile material family: overview of their properties and applications.
24B013	D.A.Balaev, A.A.Krasikov, Y.V.Knyazev*, R.N.Yaroslavtsev, D.A.Velikanov, YL.Mikhlin, M.N.Volochaev, O.A.Bayukov, V.P.Ladygina, S.V.Stolyar, and R.S.Iskhakov, <i>Nano-Struct. Nano-Objects</i> <b>37</b> ,101089(2024) Magnetic collective state formation upon tuning the interparticle interactions in ensembles of ultrafine ferrihydrite nanoparticles.
24B014	V.Bilovol, J.Zukrowski, M.Sikora, D.Errandonea, K.Berent, and M.Gajewska, <i>J. Magn. Magn. Mater.</i> <b>591</b> , 171744(2024) Effect of sintering temperature on structural, elastic, and hyperfine features of nickel ferrite nanoparticles.
24C004	A.F.Cabrera, C.E.Rodriguez Torres, and S.J.Stewart*, <i>Interactions (Cham, Switz.)</i> <b>245</b> (1),23(2024) Distinguishing nanostructured Al-doped maghemite-like $\text{Fe}_{2-y}\text{Al}_y\text{O}_3$ from spinel-like $\text{Fe}_{3-y}\text{Al}_y\text{O}_4$ .

Code	Reference
24C005	X.X.Chu, J.Chen*, F.F.Min*, Y.J.Ling, H.H.Shang, and T.Y.Wang, <i>J. Mol. Liq.</i> <b>395</b> ,123901(2024) Exploration of the interaction between Fe-doped kaolinite surface and H <sub>2</sub> O based on DFT simulation and experiment.
24D005	H.H.Ding, Y.G.Shi*, and S.L.Tang, <i>J. Rare Earths</i> <b>42</b> (4),705-9(2024) Large magnetostriction of Nd <sub>0.2</sub> Tb <sub>0.3</sub> Dy <sub>0.5</sub> Fe <sub>1.93</sub> /epoxy composites in a wide temperature range.
24D006	J.X.Ding, C.M.Tian, W.Li, J.Spielmann, C.Maheu, N.Kintop, M.Widenmeyer, K.P.Skokov, J.P.Hofmann, U.I.Kramm, W.J.Xie*, and A.Weidenkaff, <i>J. Eur. Ceram. Soc.</i> <b>44</b> (5),2972-81(2024) Tuning anisotropic thermoelectric properties of TiS <sub>2-8</sub> compounds via intercalating iron.
24D007	A.G.Dymerska, K.Wenelska, A.L.Zinnatullin, R. R.Zairov, and E.Mijowska*, <i>Electrochim. Acta</i> <b>482</b> ,144005(2024) Electroactive heterojunctions of iron-based compounds in oxygen evolution reaction-Insight into synergy and mechanism.
24D008	M.Y.Dai, S.B.Liu*, X.F.Tan*, Q.Chen, J.Ye, A.Sun, and N.Liu, <i>Sep. Purif. Technol.</i> <b>342</b> ,126841(2024) Peroxydisulfate activation by magnetic nanoflakes zero-valent iron/graphitized carbon composites for norfloxacin removal: synergistic effect of <sup>1</sup> O <sub>2</sub> with surface Fe(IV).
24D009	B.Dey, M.Bououdina, G.A.elfadeel, P. Dhamodharan, S.AsathBahadur, M.Venkateshwarlu, and C.Manoharan*, <i>J. Alloys Compd.</i> <b>970</b> ,172711(2024) Tuning the gas sensing properties of spinel ferrite NiFe <sub>2</sub> O <sub>4</sub> nanoparticles by Cu doping.
24D010	M.Dalal, J.M.Grenèche, R.S.Ningthoujam, and P.K.Chakrabarti*, <i>Mater. Chem. Phys.</i> <b>313</b> ,128765(2024) Study of magnetic induction heating of Li <sub>0.25</sub> Zn <sub>0.3</sub> Co <sub>0.15</sub> Fe <sub>2.3</sub> O nanoparticles.
24D011	Y.X.Ding, Y.M.Liu, A.Y.Klyushin, L.Y.Zhang, G.X.Han, Z.G.Liu, J.Y.Li, B.S.Zhang, K.Gao, W.Li, R.A.Eichel, X.Y.Sun*, Z.A.Qiao*, and S.Heumann, <i>Angew. Chem., Int. Ed.</i> <b>63</b> (7),e202318043/1-6(2024) Ultrathin two-dimensional layered composite carbosilicates from in situ unzipped carbon nanotubes and exfoliated bulk silica.
24D012	J.Dekan, S.Sojak, R.Hinca, Y.M.Song, V.Krsjak, M.Miklos, and J.Degmova, <i>AIP Conf. Proc.</i> <b>3054</b> (1), 050001/1-3(2024) Structural changes of FeCr alloy induced by neutron irradiation observed by Mössbauer spectrometry.
24E001	Z.El Kacemi, L.Fkhar, K.El Maalam, H.Aziam, H.Ben Youcef, I.Saadoune, A.Mahmoud, F.Boschini, O.Mounkachi, and M.Balli*, <i>J. Phys. Chem. Solids</i> <b>190</b> ,112008(2024) Downsizing and coating effects on the electrochemical performance of Mn-doped iron fluorophosphate as cathode material for sodium-ion batteries.
24E002	S.Engel, E.C.J.Gießelmann, M.K.Reimann, R.Pöttgen*, and O.Janka*, <i>ACS Org. Inorg. Au</i> <b>4</b> (2),188-222(2024) On the ytterbium valence and the physical properties in selected intermetallic phases.
24F001	M.Friak, O.Schneeweiss, J.Kamarad, J.Kaštil, O.N.Miroshkina, and M.E.Gruner, <i>J. Mater. Sci.</i> <b>59</b> (13), 5595-606(2024) Impact of swaps on Mössbauer characteristics of Ni <sub>2</sub> MnSn: an experimental and quantum-mechanical study.
24F002	S.Fernández-Velayos, G.Vergara, J.M.Olmos, J.Sanchez-Marcos, N.Menendez, P.Herrasti, and E.Mazario*, <i>Sci. Total Environ.</i> <b>906</b> ,167376(2024) A 3D printed monoliths: from powder to an efficient catalyst for antibiotic degradation.
24F003	H.Fukui, Y.Matsushi, T.Watanabe, H.Lyu, S.Kitao, Y.Kobayashi, and K.Shinoda, <i>Catena</i> <b>235</b> ,107685(2024) Redox-controlled differential weathering of andesitic pumice: possible catalytic effects of ferrous /ferric iron on rapid halloysite accumulation in a Holocene tephra layer.
24G001	M.Gracheva, Z.Klencsár, Z.Homonnay, A.Solti, L.Péter, L.Machala, P.Novak, and K.Kovács*, <i>BioMetals</i> <b>37</b> (2), 461-75(2024) Revealing the nuclearity of iron citrate complexes at biologically relevant conditions.
24G002	C.Gallenkamp, U.I.Kramm, and V.Krewald*, <i>JACS Au</i> <b>4</b> (3),940-50(2024) FeN <sub>4</sub> environments upon reduction: a computational analysis of spin states, spectroscopic properties and active species.
24G003	X.Q.Gong, Y.Liu*, R.N.He, X.Y.Xu, Z.H.Han, J.Y.Chen, B.Feng, Z.J.Wang, and A.H.Xing*, <i>ChemCatChem</i> <b>16</b> (7), e202301341/1-11(2024) Insights into the structural evolution process of Na/ZnFe <sub>2</sub> O <sub>4</sub> spinel catalyst in CO <sub>2</sub> hydrogenation.
24G004	M.Guadano-Sanchez, F.Navarro-Villoslada, G.Delgado-Soria, J.F.Marco, M.Saura-Múzquiz, L.Álvaro-Gómez, P.de la Presa, L.Perez*, and J. L.Urraca*, <i>ACS Appl. Polym. Mater.</i> <b>6</b> (6),3243-52(2024) Fast and straightforward synthesis in molecular imprinting: core-shell polymerization of magnetic imprinted polymers by microwave induction.
24G005	M.V.Goryunov, and M.I.Oshtrakh*, <i>Interactions (Cham, Switz.)</i> <b>245</b> (1),19(2024) <sup>57</sup> Fe hyperfine parameters and phase compositions in Fe-Ni-Co alloys from iron, stony-iron and stony meteorites.
24G006	S.Ghebreamlak, S.A.Stoian*, N.S.Lees, B.Cronin, F.Smith, M.O.Ross, J.Telser, B.M.Hoffman, and E.C.Duin*, <i>J. Am. Chem. Soc.</i> <b>146</b> (6),3926-42(2024) The active-site [4Fe-4S] cluster in the isoprenoid biosynthesis enzyme isph adopts unexpected redox states during ligand binding and catalysis.



Code	Reference
24G007	H.D.Guo, Y.F.Wang, and N.D.Zhang*, <i>Environ. Sci.: Water Res. Technol.</i> <b>10</b> (3),614-9(2024) Treatment of oilfield wastewater and synthesis of Na <sub>2</sub> FeO <sub>3</sub> in a chloride ion anode oxidation system.
24G008	M.Gupta, A.Das, S.Mohapatra, D.Das, S.Dutta, and A.Datta*, <i>Appl. Phys. A: Mater. Sci. Process.</i> <b>130</b> (1), 59/1-15(2024) Magnetic and Mössbauer study of lanthanum-doped nanosized cobalt ferrite assembly.
24G009	E.H.Gamage, S.Kamali, G.S.Kumar, J.K.Clark, Y.B.Lee, Y.Abusa, P.Yox, L.Q.Ke, M.Shatruk, and K.Kovnir*, <i>Inorg. Chem.</i> <b>63</b> (5),2443-53(2024) Inducing ferrimagnetic exchange in 1D-FeSe <sub>2</sub> chains using heteroleptic amine complexes: [Fe(en)(tren)][FeSe <sub>2</sub> ] <sub>2</sub> .
24G010	K.Y.Gao, J.Y.Shen, Z.Y.Lu, Y.R.Wu, Z.J.Wu, K.Shi, J.Guo, Z.Y.Wang, and M.Liu*, <i>J. Mater. Sci.: Mater. Electron.</i> <b>35</b> (3),196/1-8(2024) Calculation of special spin behavior of Dy <sup>3+</sup> in DyFe <sub>1-x</sub> Cr <sub>x</sub> O <sub>3</sub> system by molecular field model.
24H003	M.Holycross, E.Cottrell, J.Ague, A.Lanzirotti, and M.Newville, <i>Chem. Geol.</i> <b>647</b> ,121937(2024) Fe K $\alpha$ XANES, Fe K $\beta$ HERFD XANES and EPMA flank method determinations of the oxidation state of Fe in garnet.
24H004	Y.Y.Huang, Y.He, Y.Liu, J.H.Fu, X.L.Liu, X.T.Wu, and T.L.Sheng*, <i>Dalton Trans.</i> <b>53</b> (8),3777-84(2024) Fine-tuning of thermally induced SCO behaviors of trinuclear cyanido-bridged complexes by regulating the electron donating ability of CCN-terminal fragments.
24H005	M.G.Han, and Y.T.Jiang, <i>Mater. Today Commun.</i> <b>38</b> ,107693(2024) Gigahertz permeability of Fe-Cu-Nb-Si-B ferromagnetic microwires and micromagnetics simulations.
24H006	S.X.Hu, B.Zhang, J.J.Xue, and H.Pang*, <i>J. Magn. Magn. Mater.</i> <b>593</b> ,171842(2024) Lattice dynamics and enhanced electron-phonon coupling of itinerant magnet Fe <sub>1-x</sub> Co <sub>x</sub> Si (x $\geq$ 0.3): A <sup>57</sup> Fe Mössbauer spectroscopy study.
24H007	J.M.Hernandez, E.M.de la Fourniere, C.P.Ramos, M.E.Debray, R.R.Pla, R.C.Jasan, R.Invernizzi, L.G.R.Brizuela, and M.S.Canas, <i>Arch. Environ. Contam. Toxicol.</i> <b>86</b> (2),140-51(2024) Contribution of mine-derived airborne particulate matter to Ca, Fe, Mn and S content and distribution in the lichen punctelia hypoleucites transplanted to Bajo de la Alumbrera Mine, Catamarca (Argentina).
24H008	R.Harizanova, I.Mihailova, Z.P.Cherkezova-Zheleva, D.Paneva, M.Georgieva, D.Tzankov, G.Avdeev, and C.Rüssel, <i>Bol. Soc. Esp. Ceram. Vidrio</i> <b>63</b> (1),23-32(2024) Glass-crystalline materials with high iron oxide concentration: phase composition, redox ratio and magnetic properties.
24I003	A.V.Ivanova, E.V.Ivanova, A.A.Nikitin, V.M.Cherepanov, and M.A.Abakumov*, <i>J. Alloys Compd.</i> <b>976</b> , 172737(2024) Thermal decomposition of acetylacetonates for highly reproducible synthesis of M-ferrite (Mn, Co and Zn) nanoparticles with tunable magnetic properties.
24I004	O.S.Ivanova, I.S.Edelman, S.G.Ovchinnikov, A.Thakur, P.Thakur, A.L.Sukhachev, Y.V.Knyazev, R.D.Ivantsov, and M.S.Molokeev, <i>JETP Lett.</i> <b>119</b> (2),104-10(2024) Effect of cobalt concentration on the magnetic properties of the Co <sub>1-x</sub> Mg <sub>x</sub> Fe <sub>2</sub> O <sub>4</sub> nanocrystals.
24I005	A.Ibrahim, K.Tani, K.Hashi, B.F.Zhang, Z.Homonnay, E.Kuzmann, A.Bafti, L.Pavic, S.Krehula, M.Marcus, and S.Kubuki*, <i>Int. J. Mol. Sci.</i> <b>25</b> (5),2488/1-26(2024) Debye temperature evaluation for secondary battery cathode of $\alpha$ -snxfe1-xooh nanoparticles derived from the <sup>57</sup> Fe- and <sup>119</sup> Sn-Mössbauer spectra.
24J002	S.W.Jia, M.J.Shang, S.Jin, X.R.Zhu, Y.Y.Cai, and D.F.Li*, <i>Dalton Trans.</i> <b>53</b> (6),2807-14(2024) Electron transfer coupled spin transition in cyano-bridged mixed-valence {Fe <sup>III</sup> <sub>2</sub> Fe <sup>II</sup> <sub>2</sub> } molecular squares.
24J003	M.Jakubowska, K.Brzozka, M.Woźniak, J.Galazka-Friedman, and K.Szopa, <i>Interactions (Cham, Switz.)</i> <b>245</b> (1), 3(2024) The influence of sample thickness on results of Mössbauer spectroscopy of ordinary chondrites and their classification.
24J004	J.A.Jaén, M.Coronado, E.Chung, A.Munoz, M.Denvers, and G.Caballero-Manrique, <i>Interactions (Cham, Switz.)</i> <b>245</b> (1),4(2024) Structural and electrochemical characterization of tetragonal copper ferrite nanoparticles.
24K002	C.Kato, M.Ohno, T.Hatakeyama, Y.Yamada, F.Honda, K.Shimada, T.Nagase, S.Totsuka-Shiiki, Y.Kuwahara, and J.Ishibashi, <i>Phys. Chem. Miner.</i> <b>51</b> (1),5(2024) Low-temperature magnetic behavior of isocubanite from seafloor hydrothermal deposits in the Okinawa Trough.
24K003	M.S.Kilic, J.Brehme, Y.Deja, J.Pawlak, A.Günther, A.Sander, D.Müller, A.Renz, C.Rajnak, M.Polášková, B.Roth, R.F.Sindelar, and F.Renz, <i>Interactions (Cham, Switz.)</i> <b>245</b> (1),8(2024) Thin films with implemented molecular switches for the application in polymer-based optical waveguides.
24K004	D.Košovský, J.Dekan, K.Sedlacková, and M.B.Miglierini, <i>Phys. Status Solidi B</i> <b>261</b> (3),2300526/1-11(2024) Microstructure of high-chromium ferritic-martensitic steels for next-generation reactors.
24K005	O.Kaman, D.Kubaniova, L.Kubickova, V.Herynek, P.Veverka, Z.Jirak, M.Pashchenko, T.Kmjec, M.Veverka, M.Storkan, U.G.Hofmann, and J.Kohout*, <i>J. Alloys Compd.</i> <b>978</b> ,173022(2024) Magnetic particle spectroscopy and magnetic particle imaging of zinc and cobalt ferrite nanoparticles: distinct relaxation mechanisms.
24K006	I.I.Krotkii, E.Yu. Shcherbakova, S.N.Lyubchenko, N.N.Efimov, M.A.Kiskin, V.A.Lazarenko, P.A.Knyazev,

Code	Reference
	S.P.Kubrin, G.S.Borodkin, and I.N.Shcherbakov*, <i>Polyhedron</i> <b>251</b> ,116876(2024) Octahedral 3D-metal complexes of 4,6-di-tert-butyl-1,2-benzoquinone-2-monooxime: synthesis, structure, and magnetic properties.
24K007	Y.K, Y.Anvay, D.Dinakar, N.Narasaiah, V.G.Sathe, K.Kumar, and D.Haranath, <i>Ceram. Int.</i> <b>50</b> (3_Part_A), 4987-93(2024) Structural transformation and magnetic properties of Fe-substituted nano CuCr <sub>2</sub> O <sub>4</sub> spinel structure.
24K008	A.S.Komlev, E.A.Koroleva, I.D.Shabalkin, V.S.Rusakov, D.I.Komleva, T.Kiseleva, A.Y.Degtyarenko, V.I.Zverev, R.Gimaev, E.Y.Gerasimov, N.S.Perov, and P.V.Krivoshapkin, <i>Mater. Chem. Phys.</i> <b>314</b> ,128855(2024) Temperature-induced mixed magnetic states in FeRh@FeO composite nanoparticles.
24K009	L.S.Kong, G.C.Liu, Y.Liu, B.Cai, S.H.Zhan*, and J.H.Zhan*, <i>Chem. Eng. J. (Amsterdam, Neth.)</i> <b>480</b> ,148084(2024) A bioinspired iron-peroxy species of feroxyhyte for micropollutants oxidation with ultrahigh peroxymonosulfate utilization efficiency.
24K010	D.Košovský, M.B.Miglierini, T.Kmjec, M.Bujdos, and I.Janotová, <i>AIP Conf. Proc.</i> <b>3054</b> (1),020005/1-7(2024) Microstructure of high-entropy alloys.
24K011	I.Kashif, M.L.Montes, M.A.Taylor, and A.Ratep, <i>J. Mater. Sci.: Mater. Electron.</i> <b>35</b> (4),273/1-15(2024) Influence of Fe substitution on the Eu-doped lithium borosilicate glass system's physical, thermal, magnetic, and luminescent properties.
24K012	A.Krot, S.V.Savilov, E.Arkipova, and S. N.Kalmykov*, <i>J. Anal. Atom. Spectro.</i> <b>39</b> (1),71-5(2024) Stability of iron single atoms in graphene structures from X-ray absorption spectroscopy data.
24K013	K.Kozlov, V.A.Shabashov, A.Kozlov, V.Sagaradze, V.Panchenko, A.E.Zamatovskii, N.Kataeva, E.Novikov, and A.Nikitina, <i>J. Nucl. Mater.</i> <b>588</b> ,154820(2024) The effect of static stresses on the acceleration of the decomposition processes in the ferritic-martensitic steels in conditions of neutron irradiation to a dose of 85 dpa.
24L003	L.L.Lu, Q.Yan, F.G.Chen, A.Jain, H.Z.Zhou, and Y.G.Wang*, <i>Mater. Today Commun.</i> <b>38</b> ,108407(2024) Effect of trace Nb element on the performance of Fe <sub>82-x</sub> B <sub>10</sub> P <sub>7.5</sub> Cu <sub>0.5</sub> Nb <sub>x</sub> amorphous/nanocrystalline ribbons by one-step melt spinning method.
24L004	J.L.Lee, S.Biswas, J.W.Ziller, E.L.Bominaar, M.P.Hendrich, and A.S.Borovik*, <i>Chem. Sci.</i> <b>15</b> (8),2817-26(2024) Accessing a synthetic Fe <sup>III</sup> Mn <sup>IV</sup> core to model biological heterobimetallic active sites.
24L005	Q.M.Liu, H.Das*, T.Nishikubo, Y.Sakai, K.Mibu, T.Onoue, T.Kawakami, T.Watanuki, A.Machida, X.B.Ye, J.H.Dai, Z.Pan, L.Hu, S.Nakano, M.Fukuda, S.Kihara, K.Lee, T.Koike, Y.W.Long, and M.Azuma*, <i>Chem. Mater.</i> <b>36</b> (4),1899-907(2024) Pressure induced amorphization of Pb <sup>2+</sup> and Pb <sup>4+</sup> in perovskite PbFeO <sub>3</sub> .
24L006	Z.Li, H.J.Hou, Z.Y.Lu, K.Y.Gao, G.Q.Liu, Y.R.Wu, Y.J.Luo, and Y.F.Xia*, <i>Micro Nanostruct.</i> <b>188</b> ,207792(2024) Effects of manganese doping on the lattice structure and iron ion states in La <sub>2/3</sub> Ca <sub>1/3</sub> Fe <sub>1-x</sub> Mn <sub>x</sub> O <sub>3-δ</sub> .
24L007	N.A.Lomanova, I.V.Pleshakov, M. P.Volkov, S.G.Yastrebov, K.Kenges, V.L.Ugolkov, A.V.Osipov, T.Siyuan, I.VBuryanenko, and V.G.Semenov, <i>Inorg. Chem. Commun.</i> <b>161</b> ,112109(2024) Solution combustion synthesis of Bi <sub>2</sub> Fe <sub>4</sub> O <sub>9</sub> possessing enhanced magnetic and photocatalytic properties.
24L008	J.C.Li, J.Chang*, and T.Zeng, <i>ACS Appl. Nano Mater.</i> <b>7</b> (1),672-82(2024) Temperature effects on Fe(OH) <sub>3</sub> gel phase nanostructures: implications for the performance regulation and application of calcium sulfoaluminate cement.
24M002	C.Meng, W.L.Gu, B.Peng, R.Xu, H.Wang, T.Lan, G.F.Zhao, and Y.Lu*, <i>Fuel</i> <b>365</b> ,131111(2024) InNi <sub>3</sub> C <sub>0.5</sub> /Fe <sub>3</sub> O <sub>4</sub> catalyst for the CO <sub>2</sub> hydrogenation to methanol: Co-precipitation preparation, performance and mechanistic insight.
24M003	C.Mikutta, M.Niegisch, A.Thompson, R.Behrens, L.S.Schnee, M.Hoppe, and R.Dohrmann, <i>Geochim. Cosmochim. Acta</i> <b>371</b> ,126-43(2024) Redox cycling of straw-amended soil simultaneously increases iron oxide crystallinity and the content of highly disordered organo-iron(III) solids.
24M004	J.Mohammed, N.AIMasoud, K.M.Al-Ahmary, T.S.Alomar, M.R.Alrahili, H.Y.Hafeez, Z.M.El-Bahy, and A.K.Srivastava*, <i>J. Mol. Struct.</i> <b>1305</b> ,137652(2024) Hyperfine interactions, Raman spectroscopy and magnetic properties of Pr <sup>3+</sup> -Co <sup>2+</sup> substituted M-type strontium hexaferrites.
24M005	S.G.Marchetti, V.L.Barone, M.M.Torres, D.Palacios, R.C.Mercader, and E.J.Baran*, <i>Mater. Lett.</i> <b>361</b> ,136151(2024) A <sup>57</sup> Fe-Mössbauer spectroscopic study of some double and triple metal oxalates.
24M006	Y.M-Arce, M.L.Ceron, M.Alzamora, M.B.Fontes, E.Baggio-Saitovitch, and J.A.Bravo Cabrejos, <i>Interactions (Cham, Switz.)</i> <b>245</b> (1),16/1-7(2024) Clay fraction characterization of the soil profile of a quinoa plantation by X-ray diffraction and Mössbauer spectroscopy.
24M007	D.A.McKeown, H.Gan, C.Viragh, and I.L.Pegg, <i>J. Non-Cryst. Solids</i> <b>627</b> ,122812(2024) X-ray absorption spectroscopic studies of Fe environments in borosilicate waste glasses synthesized under a variety of redox conditions.



Code	Reference
24M008	E.C.Monkcom, L.Gomez, M.Lutz, S.F.Ye, E.Bill, M.Costas, and R.J.M.Klein Gebbink*, <i>Chem. - Eur. J.</i> <b>30</b> (11), e202302710/1-13(2024) Synthesis, structure and reactivity of a mononuclear N,N,O-bound Fe(II) $\alpha$ -keto-acid complex.
24M009	N.G.Mele, A.M.Guerici, and G.A.Pasquevich, <i>J. Magn. Magn. Mater.</i> <b>592</b> ,171784(2024) Cytotoxicity and genotoxicity of citric acid coated magnetite/maghemite nanoparticles in human lung cancer cells.
24O003	W.Olszewski, S.Baiju, P.Kaghazchi, C.Marini, B.Mortemard de Boisse, M.Okubo, A.Yamada, T.Mizokawa, N.L.Saini, and L.Simonelli*, <i>Mater. Today Energy</i> <b>40</b> ,101519(2024) The role of the local structural properties in the electrochemical characteristics of Na <sub>1-x</sub> Fe <sub>1-y</sub> Ni <sub>y</sub> O <sub>2</sub> cathodes.
24P001	D.A.Pankratov, E.A.Dovletyarova, A.P.Zhikharev, A.Gusev, C.Yanez, and A.Neaman*, <i>Appl. Geochem.</i> <b>166</b> , 105982(2024) Deciphering the corrosion puzzle: Nano-iron-biochar composite -Not a quick fix for metal immobilization in peat soils.
24P002	G.S.Paronetto, M.S.Olivelli, M.L.Montes, M.A.Fernandez, V.C.Delfosse, J.L.Marco-Brown*, and R.Candal, <i>Ind. Eng. Chem. Res.</i> <b>63</b> (4),1893-902(2024) One pot green synthesis of supported reductive biogenic iron-based materials for the removal of chromium(VI).
24R001	D.H.Ryan, B.Kuthanazhi, N.H.Jo, and P.C.Canfield, <i>AIP Adv.</i> <b>14</b> (1),015239/1-5(2024) Complex magnetic ordering in EuAl <sub>4</sub> -A <sup>151</sup> Eu Mössbauer study.
24T003	L. M.Tran, A.J.Zaleski, and Z.Bukowski, <i>Phys. Rev. B</i> <b>109</b> (1),014509/1-9(2024) Reentrant resistivity due to the interplay of superconductivity and magnetism in Eu <sub>0.73</sub> Ca <sub>0.27</sub> (Fe <sub>0.87</sub> Co <sub>0.13</sub> ) <sub>2</sub> As <sub>2</sub> .
24Y001	S.Y.Yang, J.J.Xue, B.Zhang, P.Wu, Y.W.Dong, Z.W.Li, F.S.Li, and L.Qiao*, <i>AIP Adv.</i> <b>14</b> (1),015146/1-9(2024) Exploring phase formation and magnetic transitions in Sm(Fe <sub>1-x</sub> Mn <sub>x</sub> ) <sub>14</sub> B by Mössbauer spectroscopy.
24Z003	X.Zhang, J.J.Tang, L.L.Wang, C.Wang, L.Chen, X.Q.Chen, J.S.Qian*, and B.C.Pan*, <i>Nat. Commun.</i> <b>15</b> (1), 917(2024) Nanoconfinement-triggered oligomerization pathway for efficient removal of phenolic pollutants via a Fenton-like reaction.
24Z004	I.Y.Zavaliy, I.V.Koval'chuck, R.V.Denys, R.Cerny, V.K.Pecharsky, and P.Zavalij, <i>J. Alloys Compd.</i> <b>980</b> , 173531(2024) H-Induced local disorder in the structure of Ti <sub>2</sub> Ni-type Hf(Zr) <sub>4</sub> Fe <sub>2</sub> O <sub>x</sub> compounds.

Source	Absorber	Temp	IS	QS	Comments	Code
<u>Eu-151 21.60 keV Transition</u>						
xx	Eu <sub>0.73</sub> Ca <sub>0.27</sub> (Fe <sub>0.87</sub> Co <sub>0.13</sub> ) <sub>2</sub> As <sub>2</sub>	v	--	--	reviewed the previously studied Mössbauer effect and compared with presently studied magnetic and other properties	24T003
xx(IS/ $\alpha$ -Fe)	EuAl <sub>4</sub> and EuGa <sub>4</sub>	v	--	--	identified several magnetic phase transitions and magnetic structure changes with temperature and determined corresponding T <sub>N</sub> values	24R001
<u>Fe-57 14.40 keV Transition: Biological Compounds</u>						
Rh(IS/ $\alpha$ -Fe)	airborne particulate matter in the lichen Punctelia hypoleucites (Argentina)	v	--	--	determined the presence of pyrite (FeS <sub>2</sub> ) and ferrous sulfate particles	24H007
xx(IS/ $\alpha$ -Fe)	Ascorbate Peroxidase Compound II	298	0.05	1.66	calculated Mössbauer and NRVS parameters for all Fe(IV)-oxo/hydroxo models using the B3LYP functional, and compared to experimental Mössbauer data for APX-II	24A008
Rh(IS/ $\alpha$ -Fe)	Biogenic iron oxide particles alone and supported on montmorillonite (BioFe and BioFe-MMT)	300	--	--	identified several Fe <sup>3+</sup> and Fe <sup>2+</sup> subspectra and determined the relative abundances of Fe <sup>2+</sup> and Fe <sup>3+</sup>	24P002
Rh(IS/ $\alpha$ -Fe)	citric-acid-coated magnetite/maghemite nanoparticles	300	--	--	identified magnetite-like and maghemite-like fractions with a relative abundance of 57 % maghemite and 43 % magnetite	24M009
Rh(IS/ $\alpha$ -Fe)	collected from the different weathering zones andesitic pumice: greyish weathered pumice (GP), white weathered pumice (WP), and brownish weathered pumice of Lake Shikotsu	v	--	--	determined the relative abundances of Fe <sup>2+</sup> and Fe <sup>3+</sup>	24F003
Rh(IS/ $\alpha$ -Fe)	dithionite	4.2	--	--	in the reduced [4Fe-4S] <sup>+</sup> cluster, determined the parameters of the states of 7 cluster sites with S=0 (3 sites, 19%), S=1/2 (2 sites, 37%), and S=3/2 (2 sites, 44%)	24G006
Rh(IS/ $\alpha$ -Fe)	initial iron powder and nano-iron-biochar and their corrosion products after one month of humidity exposure in cellulose and in peat	v	--	--	identified alpha and gamma iron, alpha and gamma FeOOH and theta-Fe <sub>3</sub> C	24P001
Rh(IS/ $\alpha$ -Fe)	primary sludges and digested sludges of wastewater from Viikimäki (Finland) and Seine Aval (France)	v	--	--	identified vivianite subspectra and other probable major contributors such as poorly formed ferrihydrite, goethite, and hematite	24A007
Rh(IS/ $\alpha$ -Fe)	ultrafine two-line-ferrihydrite nanoparticles with varying magnetic interparticle interactions strength tuned by coating	v	--	--	determined the relaxation times to compare with the data determined by static and dynamic magnetic susceptibilities	24B013
Rh(IS/ $\alpha$ -Fe)	[ <sup>57</sup> Fe <sup>III</sup> (O)Mn <sup>III</sup> poat] <sup>+</sup> in PrCN and [ <sup>57</sup> Fe <sup>III</sup> (O)Mn <sup>IV</sup> poat] <sup>2+</sup> in PrCN	4.2	--	--	first quantitative demonstration of the effect of the hyperfine interaction from a non-Fe nucleus on the Mössbauer spectra	24L004
Rh(IS/ $\alpha$ -Fe)	$\delta$ -FeOOH nanosheets	14	--	--	identified abundant 5-coordinated iron sites in $\delta$ -FeOOH and confirmed the iron-peroxy species	24K009
<u>Fe-57 14.40 keV Transition: Catalysts</u>						
Rh(IS/ $\alpha$ -Fe)	citric-acid-coated magnetite/maghemite nanoparticles	300	--	--	identified magnetite-like and maghemite-like fractions with a relative abundance of 57 % maghemite and 43 % magnetite	24M009
Rh(IS/ $\alpha$ -Fe)	combustion synthesized Bi <sub>2</sub> Fe <sub>4</sub> O <sub>9</sub>	300	--	--	identified 2 doublets with IS values of tetrahedral sites and octahedral sites with approximate equal occupancy	24L007
Rh(IS/ $\alpha$ -Fe)	coprecipitated catalysts Fe-cp, FeZn-cp, and FeZn-2.8Na before and after 100 h FT reaction	300	--	--	identified in the spent catalysts the phases of Fe <sub>3</sub> O <sub>4</sub> , Fe <sub>3</sub> C <sub>2</sub> , Fe <sub>7</sub> C <sub>3</sub> , and spm-Fe <sup>3+</sup>	24G003
P01 High Resolution Dynamics beamline at PETRA III (DESY)	Fe-N-C catalysts	v	--	--	performed a tutorial review of the NFS method and HER reaction in situ and operando nuclear forward scattering experiments at different potentials and conditions	23H037
Rh(IS/ $\alpha$ -Fe)	Fenton catalysts UiO-66-NH <sub>2</sub> -(Zr/Fe) nanoparticles unsupported and supported on the graphene aerogel substrate	300	--	--	the supported catalysts exhibit a larger quadrupole splitting (QS) (0.662mm·s <sup>-1</sup> ) compared to unsupported (QS=0.584mm·s <sup>-1</sup> ); the increased QS is attributed to a more distorted site	24Z003
Rh(IS/ $\alpha$ -Fe)	InNi <sub>3</sub> C <sub>0.5</sub> /Fe <sub>3</sub> O <sub>4</sub> catalyst	v	--	--	identified A and B sextets of Fe <sub>3</sub> O <sub>4</sub>	24M002

Source	Absorber	Temp	IS	QS	Comments	Code
Rh(IS/ $\alpha$ -Fe)	molecular imprint polymer-coated magnetic multicore (MIP-MMC) iron oxide nanoparticles	8.5	--	--	identified 5 sextets consistent with those reported for magnetite nanoparticles of comparable sizes	24G004
Rh(IS/ $\alpha$ -Fe)	mononuclear benzoylformate complex, [Fe(Im <sup>Ph2</sup> NNO <sup>tBu</sup> )(BF)]	80	1.17	2.64	identified N,N,O-bound iron(II) pentacoordinate site, similar to O <sub>2</sub> -reactive active sites of $\alpha$ KG-dependent iron enzymes	24M008
Rh(IS/ $\alpha$ -Fe)	Ni/Fe-based catalysts before and after in-situ reduction in H <sub>2</sub> /Ar gas at 250°C for the times: 0.5, 1.0, 2.0, 3.0, and 4.0 h	300	--	--	identified ferrihydrite, spinel magnetic and superparamagnetic iron oxide and Fe <sub>3</sub> C	24D007
Rh(IS/ $\alpha$ -Fe)	powder blend of iron oxide and polylactic acid (PLA) at 15 wt% of Fe-oxide, single monolith 15%-Fe <sub>3</sub> O <sub>4</sub> @PLA	300	--	--	identified two Zeeman sextet assigned to Fe <sup>3+</sup> in A and B sites with a hyperfine field and isomer shift associated with each position are measured as 44.4 T (IS=0.388 mm/s) and 48.5 T (IS=0.321 mm/s)	24F002
xx(IS/ $\alpha$ -Fe)	pure Na <sub>2</sub> Fe <sub>0.5</sub> Mn <sub>0.5</sub> PO <sub>4</sub> F and dopamine-coated Na <sub>2</sub> Fe <sub>0.5</sub> Mn <sub>0.5</sub> PO <sub>4</sub> F	v	--	--	identified both Fe(II) and Fe(III) before coating and only Fe(II) after coating	24E001
Rh(IS/ $\alpha$ -Fe)	raw iron-biochar composite Fe@SBC <sub>1.13</sub> and after reaction with peroxydisulfate (PDS) activator: Fe@SBC <sub>1.13</sub> /PDS	300	--	--	a new doublet with a $\delta$ value of -0.19 mm s <sup>-1</sup> was detected when a small quantity of PDS solution was introduced into the system	24D008
Rh(IS/ $\alpha$ -Fe)	[Fe(TPP)Cl] and [Fe(phen <sub>2</sub> N <sub>2</sub> )Cl], where TPP= tetraphenylporphyrin and phen =1,10-phenanthroline	v	--	--	reviewed and calculated the QS and IS parameters and vibrational spectra of iron ions in the formal oxidation states +II and +III with and without an axial ligand for pyridinic and pyrrolic environments	24G002
Rh(IS/ $\alpha$ -Fe)	$\delta$ -FeOOH nanosheets	14	--	--	identified abundant 5-coordinated iron sites in $\delta$ -FeOOH and confirmed the iron-peroxy species	24K009
<u>Fe-57 14.40 keV Transition: FERROMAGNETIC</u>						
Rh(IS/ $\alpha$ -Fe)	Co <sub>1-x</sub> Mg <sub>x</sub> Fe <sub>2</sub> O <sub>4</sub> nanocrystals	300	--	--	identified a Fe <sub>2</sub> O <sub>3</sub> impurity and in spinel nanocrystals Fe(III) distributions : the contents of 6-coordinated Fe(III) and 4-coordinated Fe(III)	24I004
Rh(IS/ $\alpha$ -Fe)	CuCr <sub>1.5</sub> Fe <sub>0.5</sub> O <sub>4</sub> and CuCr <sub>0.5</sub> Fe <sub>1.5</sub> O <sub>4</sub>	300	--	--	identified trivalent state pf iron	24K007
Rh(IS/ $\alpha$ -Fe)	heteroleptic amine complex [Fe(en)(tren)][FeSe <sub>2</sub> ] <sub>2</sub> (en=ethylenediamine, C <sub>2</sub> H <sub>8</sub> N <sub>2</sub> , tren=tris(2-aminoethyl)amine, C <sub>6</sub> H <sub>18</sub> N <sub>4</sub> )	v	--	--	identified components with the ratio between the intensities approximately 2:1, and confirmed the separation of Fe <sup>3+</sup> and Fe <sup>2+</sup> sublattices	24G009
Rh(IS/ $\alpha$ -Fe)	La <sub>2/3</sub> Ca <sub>1/3</sub> Fe <sub>1-x</sub> Mn <sub>x</sub> O <sub>3-<math>\delta</math></sub> ( $x = 0-0.6$ )	300	--	--	with increase in the amount of Mn doping the proportion of antiferromagnetic sextets decreases	24L006
Rh(IS/ $\alpha$ -Fe)	Li <sub>0.25</sub> Zn <sub>0.3</sub> Co <sub>0.15</sub> Fe <sub>2.3</sub> O nanoparticles annealed at 200, 500, 600, 700 and 800 °C for 5 h in air	v	--	--	assumed 5 sextet components, suggesting the presence of nanoparticles with different sizes, and a quadrupolar smp-doublet up to 12%	24D010
Rh(IS/ $\alpha$ -Fe)	M-ferrites (M=Mn, Co and Zn, M:Fe=1:2 $\pm$ 0.1)	300	--	--	application of a weak magnetic field (Ha=3.4 kOe) led to a partial restoration of the magnetic hyperfine structure	24I003
Rh(IS/ $\alpha$ -Fe)	nanocrystalline ferromagnetic Fe-Cu-Nb-Si-B microwires	298	--	--	observed two kinds of components: a ferromagnetic related to the distribution of hyperfine fields for amorphous phase, and other one is the discrete subspectra components for nanograins with narrow sextet lines	24H005
Rh(IS/ $\alpha$ -Fe)	nanostructured Al-doped Fe <sub>2-<math>y</math></sub> Al <sub><math>y</math></sub> O <sub>3</sub> ( $x = 0.33$ ) prepared by the autocombustion method	13	--	--	identified 3 sextets and 2 doublets, of which only minor doublet (4%) is assigned to Fe <sup>2+</sup>	24C004
Rh(IS/ $\alpha$ -Fe)	PbFeO <sub>3</sub>	300	--	--	identified three sets of magnetic sextets, which are attributed to Fe at the 16h and 8d sites, and to the $\alpha$ -Fe <sub>2</sub> O <sub>3</sub> impurity	24L005
Rh(IS/ $\alpha$ -Fe)	pristine and milled BaTi <sub>0.90</sub> Fe <sub>0.10</sub> O <sub>3-<math>\delta</math></sub>	300	--	--	observed three kinds of components: one or two ferromagnetic, antiferromagnetic and paramagnetic	24B011
Rh(IS/ $\alpha$ -Fe)	Sm <sub>2</sub> (Fe <sub>1-x</sub> Mn <sub>x</sub> ) <sub>14</sub> B ( $0 \leq x \leq 0.3$ )	v	--	--	identified magnetic sextets and partially or fully collapsed spectral signatures of the sites 16k <sub>1</sub> , 16k <sub>2</sub> , 8j <sub>1</sub> , 8j <sub>2</sub> , 4c, 4e	24Y001
Rh(IS/ $\alpha$ -Fe)	ultrafine two-line-ferrihydrite nanoparticles with varying magnetic interparticle interactions strength tuned by coating	v	--	--	determined the relaxation times to compare with the data determined by static and dynamic magnetic susceptibilities	24B013
TmB <sub>12</sub>	Yb <sub>3</sub> Cu <sub>4</sub> Ge <sub>4</sub>	v	--	--	reviewed paramagnetic and Zeeman-split spectra and magnetic behavior of Yb <sub>3</sub> Cu <sub>4</sub> Ge <sub>4</sub> and Gd <sub>3</sub> Cu <sub>4</sub> Ge <sub>4</sub> and hyperfine parameters in many other intermetallic ytterbium compounds	24E002

Source	Absorber	Temp	IS	QS	Comments	Code
<u>Fe-57 14.40 keV Transition: Frozen Solutions</u>						
Rh(IS/ $\alpha$ -Fe)	iron(III) citrate frozen solutions at different Fe to citrate molar ratios	5	--	--	confirmed the coexistence of several monoiron species with different coordination environments	24G001
<u>Fe-57 14.40 keV Transition: Glasses and Amorphous Substances</u>						
Rh(IS/ $\alpha$ -Fe)	borosilicate waste glasses synthesized under a variety of redox conditions	300	--	--	measured Fe <sup>2+</sup> /Fe(total) ratio to compare with XANES data	24M007
Rh(IS/ $\alpha$ -Fe)	Fe substituted Eu-doped lithium borosilicate glass (30% Li <sub>2</sub> O, 40% B <sub>2</sub> O <sub>3</sub> , 25% SiO <sub>2</sub> )	300	--	--	identified major Fe <sup>3+</sup> doublets assigned to 2 kinds of sites (tetra and octa) and minor Fe <sup>2+</sup> and Fe <sup>2+/3+</sup>	24K011
xx(IS/ $\alpha$ -Fe)	Fe <sub>82-x</sub> B <sub>10</sub> P <sub>7.5</sub> Cu <sub>0.5</sub> Nb <sub>x</sub> ( $x = 0, 0.5, 1.0, \& 1.5$ ) alloy ribbons	v	--	--	identified a broadened sextet with enhanced lines 2 and 5 suggesting a preferred orientation of easy magnetization axis	24L003
Rh(IS/ $\alpha$ -Fe)	Fenton catalysts UiO-66-NH <sub>2</sub> -(Zr/Fe) nanoparticles unsupported and supported on the graphene aerogel substrate	300	--	--	the supported catalysts exhibit a larger quadrupole splitting (QS) (0.662mm·s <sup>-1</sup> ) compared to unsupported (QS=0.584mm·s <sup>-1</sup> ); the increased QS is attributed to a more distorted site	24Z003
Rh(IS/ $\alpha$ -Fe)	iron phosphate glasses	300	--	--	identified components assigned to Fe <sup>2+</sup> and two sites of Fe <sup>3+</sup> : Td and Oh	24A005
Rh(IS/ $\alpha$ -Fe)	nanocrystalline ferromagnetic Fe-Cu-Nb-Si-B microwires	298	--	--	observed two kinds of components: a ferromagnetic related to the distribution of hyperfine fields for amorphous phase, and other one is the discrete subspectra components for nanograins with narrow sextet lines	24H005
<u>Fe-57 14.40 keV Transition: Inorganic Cyanides</u>						
Rh(IS/ $\alpha$ -Fe)	mononuclear benzoylformate complex, [Fe(Im <sup>Ph2</sup> NNO <sup>Bu</sup> )(BF)]	80	1.17	2.64	identified N,N,O-bound iron(II) pentacoordinate site, similar to O <sub>2</sub> -reactive active sites of $\alpha$ KG-dependent iron enzymes	24M008
Rh(IS/ $\alpha$ -Fe)	trinuclear cyanido-bridged complexes	v	--	--	identified Fe(II) LS and Fe(II) HS in two structure sites	24H004
Rh(IS/ $\alpha$ -Fe)	[ <sup>57</sup> Fe <sup>III</sup> (O)Mn <sup>III</sup> poat] <sup>+</sup> in PrCN and [ <sup>57</sup> Fe <sup>III</sup> (O)Mn <sup>IV</sup> poat] <sup>2+</sup> in PrCN	4.2	--	--	first quantitative demonstration of the effect of the hyperfine interaction from a non-Fe nucleus on the Mössbauer spectra	24L004
Rh(IS/ $\alpha$ -Fe)	{[Fe(Tp)(CN) <sub>3</sub> ] <sub>2</sub> [Fe(bnbpen) <sub>2</sub> ](ClO <sub>4</sub> ) <sub>2</sub> ·8CH <sub>3</sub> OH (bnbpen = N,N-bis-(2-naphthylmethyl)-N,N-bis(2-picolyl)-ethylenediamine)}	v	--	--	identified both Fe(II)LS and Fe(II)HS and Fe(III) components and observed a thermal ETCST process involving the transformation of {Fe <sup>III</sup> ,LS( $\mu$ -CN)Fe <sup>II</sup> ,HS} <sub>2</sub> (HT phase) and {Fe <sup>II</sup> ,LS( $\mu$ -CN)Fe <sup>III</sup> ,LS} <sub>2</sub> (LT phase)	24J002
<u>Fe-57 14.40 keV Transition: Inorganic Oxides</u>						
Rh(IS/ $\alpha$ -Fe)	4-CaO·Al <sub>2</sub> O <sub>3</sub> ·Fe <sub>2</sub> O <sub>3</sub> hydrated at temperatures of 5 °C and 90 °C for 28 days	300	--	--	identified three of Fe <sup>3+</sup> doublets assigned to tetra (one site) and octa (two sites) coordinations; the tetra-site population decreases with increasing hydration temperature	24L008
Rh(IS/ $\alpha$ -Fe)	<sup>57</sup> Fe <sub>0.004</sub> Mn <sub>0.096</sub> ScO <sub>3</sub>	16	0.42	0.13	all probe Fe-atoms occupy equivalent crystallographic and magnetic positions   MF=47.9 T	23S094
Rh(IS/ $\alpha$ -Fe)	borosilicate waste glasses synthesized under a variety of redox conditions	300	--	--	measured Fe <sup>2+</sup> /Fe(total) ratio to compare with XANES data	24M007
Rh(IS/ $\alpha$ -Fe)	citric-acid-coated magnetite/maghemite nanoparticles	300	--	--	identified magnetite-like and maghemite-like fractions with a relative abundance of 57 % maghemite and 43 % magnetite	24M009
Rh(IS/ $\alpha$ -Fe)	Co <sub>1-x</sub> Mg <sub>x</sub> Fe <sub>2</sub> O <sub>4</sub> nanocrystals	300	--	--	identified a Fe <sub>2</sub> O <sub>3</sub> impurity and in spinel nanocrystals Fe(III) distributions: the contents of 6-coordinated Fe(III) and 4-coordinated Fe(III)	24I004
Rh(IS/ $\alpha$ -Fe)	CoFe <sub>(2-x)</sub> La <sub>x</sub> O <sub>4</sub> ( $x=0, 0.05, 0.10, 0.15$ )	300	--	--	there exists an upper limit of La inclusion in the ferrite matrix	24G008
Rh(IS/ $\alpha$ -Fe)	collected from the different weathering zones andesitic pumice: greyish weathered pumice (GP), white weathered pumice (WP), and brownish weathered pumice of Lake Shikotsu	v	--	--	determined the relative abundances of Fe <sup>2+</sup> and Fe <sup>3+</sup>	24F003
Rh(IS/ $\alpha$ -Fe)	combustion synthesized Bi <sub>2</sub> Fe <sub>4</sub> O <sub>9</sub>	300	--	--	identified 2 doublets with IS values of tetrahedral sites and octahedral sites with approximate equal occupancy	24L007
Rh(IS/ $\alpha$ -Fe)	Composites 10%NiFe <sub>2</sub> O <sub>4</sub> @HPPE, 20%NiFe <sub>2</sub> O <sub>4</sub> @HPPE, 30%NiFe <sub>2</sub> O <sub>4</sub> @HPPE (HPPE = High-pressure polyethylene)	14	--	--	as the nickel ferrite content increases from 10 to 20 and 30 wt.%, the iron ion population in the A site of NiFe <sub>2</sub> O <sub>4</sub> increases from 45% to 52% and 64%	23Y024

Source	Absorber	Temp	IS	QS	Comments	Code
Rh(IS/ $\alpha$ -Fe)	core/shell FeRh@FeO nanoparticles	v	--	--	identified both magnetic and spm-components in both alloys and iron oxides or/and iron oxyhydroxides phases	24K008
Rh(IS/ $\alpha$ -Fe)	Cu <sub>0.5</sub> Ni <sub>0.5</sub> Fe <sub>2</sub> O <sub>4</sub> and Ni <sub>1-x</sub> Cu <sub>x</sub> Fe <sub>2</sub> O <sub>4</sub> nanoparticles (x=0.0, 0.1, 0.3)	300	--	--	identified two sextets (A and B-sites) and a minor spm-component	24D009
Rh(IS/ $\alpha$ -Fe)	CuCr <sub>1.5</sub> Fe <sub>0.5</sub> O <sub>4</sub> and CuCr <sub>0.5</sub> Fe <sub>1.5</sub> O <sub>4</sub>	300	--	--	identified trivalent state pf iron	24K007
Rh(IS/ $\alpha$ -Fe)	DyFe <sub>0.1</sub> Cr <sub>0.9</sub> O <sub>3</sub> synthesized by sol-gel	300	0.216	0.256	identified only one doublet (octa-sites) of Fe(III) HS	24G010
Rh(IS/ $\alpha$ -Fe)	DyFe <sub>0.9</sub> Cr <sub>0.1</sub> O <sub>3</sub> synthesized by sol-gel	300	0.244	0.004	identified only one sextet (octa-sites) of Fe(III) HS   MF = 49.516 T	24G010
Rh(IS/ $\alpha$ -Fe)	DyFe <sub>x</sub> Mn <sub>1-x</sub> O <sub>3</sub> (x=0.1, 0.3, 0.5, 0.7, 0.9, and 1.0)	v	--	--	identified between 295 K and 78 K the paramagnetic nature for x $\leq$ 0.3, while magnetic nature for x $\geq$ 0.7	24B010
Rh(IS/ $\alpha$ -Fe)	Fe substituted Eu-doped lithium borosilicate glass (30% Li <sub>2</sub> O, 40% B <sub>2</sub> O <sub>3</sub> , 25% SiO <sub>2</sub> )	300	--	--	identified major Fe <sup>3+</sup> doublets assigned to 2 kinds of sites (tetra and octa) and minor Fe <sup>2+</sup> and Fe <sup>2+/3+</sup>	24K011
Rh(IS/ $\alpha$ -Fe)	Fe-doped kaolinite	300	--	--	identified a doublet of Fe(II) and two doublets of Fe(III) : 6-coordination Fe(III) and 4-coordination Fe(III)	24C005
Rh(IS/ $\alpha$ -Fe)	ferrites Co <sub>0.68</sub> Fe <sub>2.3</sub> O <sub>4</sub> , Co <sub>1.06</sub> Fe <sub>1.94</sub> O <sub>4</sub> , Zn <sub>0.34</sub> Fe <sub>2.51</sub> O <sub>4</sub> , Zn <sub>0.32</sub> Fe <sub>2.52</sub> O <sub>4</sub>	4.2	--	--	under magnetic field of 6 T identified seven sextes, which account for the distribution of Fe <sup>3+</sup> and Fe <sup>2+</sup> with Zn or Co and vacancies in their second coordination sphere	24K005
xx	Garnet reference materials from Museum of Natural History, Smithsonian Institution	300	--	--	identified Fe <sup>2+</sup> and Fe <sup>3+</sup> and determined Fe <sup>3+</sup> /ΣFe ratios to compare with Fe <sup>3+</sup> /ΣFe from Fe L $\alpha$ and Fe L $\beta$ emission lines and with Fe <sup>3+</sup> /ΣFe from XANES	24H003
Rh(IS/ $\alpha$ -Fe)	glass-crystalline materials in the system Na <sub>2</sub> O/CaO/SiO <sub>2</sub> /Fe <sub>2</sub> O <sub>3</sub> with the Fe <sub>2</sub> O <sub>3</sub> concentrations of 20, 25 and 30 mol%	300	--	--	identified doublets of Fe <sup>3+</sup> and Fe <sup>2+</sup> and up to 7 sextets assigned to epsilon-Fe <sub>2</sub> O <sub>3</sub> and spinel phases	24H008
Rh(IS/ $\alpha$ -Fe)	InNi <sub>3</sub> C <sub>0.5</sub> /Fe <sub>3</sub> O <sub>4</sub> catalyst	v	--	--	identified A and B sextets of Fe <sub>3</sub> O <sub>4</sub>	24M002
Rh(IS/ $\alpha$ -Fe)	iron meteorites Anyujskij IIAB and Gibeon IVA, stony-iron meteorite Seymchan PMG and stony meteorites Annama H5 and Kemer L4	295	--	--	determined Fe hyperfine parameters in the phases $\alpha^2$ -Fe(Ni, Co), $\alpha$ -Fe(Ni, Co), $\gamma$ -Fe(Ni, Co) and $\gamma$ -FeNi(Co)	24G005
Rh(IS/ $\alpha$ -Fe)	iron phosphate glasses	300	--	--	identified components assigned to Fe <sup>2+</sup> and two sites of Fe <sup>3+</sup> : Td and Oh	24A005
Rh(IS/ $\alpha$ -Fe)	isocubanite from seafloor hydrothermal deposits in the Okinawa Trough before and after heating	v	--	--	identified sites 1 and 2 of CuFe <sub>3</sub> S <sub>4</sub> and chalcopyrite	24K002
Rh(IS/ $\alpha$ -Fe)	Jilin meteorite	300	--	--	sample thickness in ordinary chondrite has no effect on percentages of Mössbauer spectral areas of troilite and FeNi alloy (kamacite and taenite) and olivine and pyroxene	24J003
Rh(IS/ $\alpha$ -Fe)	La <sub>2/3</sub> Ca <sub>1/3</sub> Fe <sub>1-x</sub> Mn <sub>x</sub> O <sub>3-<math>\delta</math></sub> (x = 0–0.6)	300	--	--	with increase in the amount of Mn doping the proportion of antiferromagnetic sextets decreases	24L006
Rh(IS/ $\alpha$ -Fe)	layered carbosilicate formed from CNT with up to 10 wt% iron content (10Fe-CSiO <sub>x</sub> ) compared to iron silicate without carbon	80	--	--	identified 85% of Fe <sup>3+</sup> and 15% of Fe <sup>2+</sup> in 10Fe-CSiO <sub>x</sub> , while 100% of Fe <sup>3+</sup> in iron silicate without carbon	24D011
Rh(IS/ $\alpha$ -Fe)	Li <sub>0.25</sub> Zn <sub>0.3</sub> Co <sub>0.15</sub> Fe <sub>2.3</sub> O nanoparticles annealed at 200, 500, 600, 700 and 800 °C for 5 h in air	v	--	--	assumed 5 sextet components, suggesting the presence of nanoparticles with different sizes, and a quadrupolar smp-doublet up to 12%	24D010
Rh(IS/ $\alpha$ -Fe)	Loess-soil from the Terek–Kuma lowland	v	--	--	identified goethite and hematite and several doublets assigned to Fe <sup>2+</sup> and Fe <sup>3+</sup> and determined the ratio of Fe <sup>2+</sup> /(Fe <sup>3+</sup> + Fe <sup>2+</sup> )	24A006
Rh(IS/ $\alpha$ -Fe)	M-ferrires (M=Mn, Co and Zn, M:Fe=1:2 $\pm$ 0.1)	300	--	--	application of a weak magnetic field (Ha=3.4 kOe) led to a partial restoration of the magnetic hyperfine structure	24I003
Rh(IS/ $\alpha$ -Fe)	M-type strontium hexaferrites Sr <sub>1-x</sub> Pr <sub>x</sub> Fe <sub>12-y</sub> Co <sub>y</sub> O <sub>19</sub> (x=0.0, 0.2, 0.4 and y = 0.0, 0.15, 0.35)	300	--	--	identified the sextet contributions assigned to 12k, 4f <sub>2</sub> , 4f <sub>1</sub> , 2a, as well as 2b sites	24M004
Rh(IS/ $\alpha$ -Fe)	manganite In <sub>0.97</sub> (Mn <sub>0.99</sub> <sup>57</sup> Fe <sub>0.01</sub> ) <sub>1.03</sub> O <sub>3</sub>	16	0.38	0.26	all probe iron cations demonstrate the magnetic hyperfine structure of the nuclear levels, i.e., indicate the formation of a magnetically ordered state   MF = 46.7 T	23S094
Rh(IS/ $\alpha$ -Fe)	manganites <sup>57</sup> Fe <sub>0.008</sub> Mn <sub>1.992</sub> O <sub>3</sub> , <sup>57</sup> Fe <sub>0.004</sub> Mn <sub>0.996</sub> ScO <sub>3</sub> and In <sub>0.97</sub> (Mn <sub>0.99</sub> <sup>57</sup> Fe <sub>0.01</sub> ) <sub>1.03</sub> O <sub>3</sub>	298	--	--	identified equipopulated Fe(1) and Fe(2) sites in Mn <sub>2</sub> O <sub>3</sub> , a single Fe(1) site in ScMnO <sub>3</sub> and unequally populated Fe(1)-92% and Fe(2) (8% of Fe in In site) for FeInO <sub>3</sub>	23S094

Source	Absorber	Temp	IS	QS	Comments	Code
Rh(IS/ $\alpha$ -Fe)	Mg <sub>1/3</sub> Ni <sub>1/3</sub> Co <sub>1/3</sub> Fe <sub>2-x</sub> La <sub>x</sub> O <sub>4</sub>	77	--	--	identified two sextets with hyperfine fields decreasing from $53.6 \pm 0.5$ and $50.0 \pm 0.5$ T for $x = 0$ to $52.9 \pm 0.5$ and $46.0 \pm 0.5$ T for $x = 0.08$	24A010
Rh(IS/ $\alpha$ -Fe)	molecular imprint polymer-coated magnetic multicore (MIP-MMC) iron oxide nanoparticles	8.5	--	--	identified 5 sextets consistent with those reported for magnetite nanoparticles of comparable sizes	24G004
Rh(IS/ $\alpha$ -Fe)	nanoparticles of $\alpha$ -FeOOH, $\alpha$ -Sn <sub>0.10</sub> Fe <sub>0.90</sub> OOH, $\alpha$ -Sn <sub>0.15</sub> Fe <sub>0.85</sub> OOH, and $\alpha$ -Sn <sub>0.2</sub> Fe <sub>0.8</sub> OOH	v	--	--	identified the magnetic and superparamagnetic goethite phases and an unknown component	24I005
Rh(IS/ $\alpha$ -Fe)	nanostructured Al-doped Fe <sub>2-y</sub> Al <sub>y</sub> O <sub>3</sub> ( $x=0.33$ ) prepared by the autocombustion method	13	--	--	identified 3 sextets and 2 doublets, of which only minor doublet (4%) is assigned to Fe <sup>2+</sup>	24C004
Rh(IS/ $\alpha$ -Fe)	Ni/Fe-based catalysts before and after in-situ reduction in H <sub>2</sub> /Ar gas at 250 °C for the times: 0.5, 1.0, 2.0, 3.0, and 4.0 h	300	--	--	identified ferrihydrite, spinel magnetic and superparamagnetic iron oxide and Fe <sub>3</sub> C	24D007
Rh(IS/ $\alpha$ -Fe)	NiFe <sub>2</sub> O <sub>4</sub> annealed for 4 h at 573 K, 873 K, and 1073 K	300	--	--	identified two doublets (A and B sites) for annealing at 573K and two sextets for annealing at 873 K and 1073 K	24A009
xx(IS/ $\alpha$ -Fe)	NiFe <sub>2</sub> O <sub>4</sub> nanoparticles synthesized by a chemical coprecipitation method at temperatures of 500, 600, 700, 900, and 1000 °C	300	--	--	the population of A-sites decreases with increasing annealing temperature, and the population of B-sites increases with increasing annealing temperature	24B014
Rh(IS/ $\alpha$ -Fe)	PbFeO <sub>3</sub>	300	--	--	identified three sets of magnetic sextets, which are attributed to Fe at the 16h and 8d sites, and to the $\alpha$ -Fe <sub>2</sub> O <sub>3</sub> impurity	24L005
Rh(IS/ $\alpha$ -Fe)	powder blend of iron oxide and polylactic acid (PLA) at 15 wt% of Fe-oxide, single monolith 15%-Fe <sub>3</sub> O <sub>4</sub> @PLA	300	--	--	identified two Zeeman sextet assigned to Fe <sup>3+</sup> in A and B sites with a hyperfine field and isomer shift associated with each position are measured as 44.4 T (IS = 0.388 mm/s) and 48.5 T (IS = 0.321 mm/s)	24F002
Rh(IS/ $\alpha$ -Fe)	primary sludges and digested sludges of wastewater from Viikimäki (Finland) and Seine Aval (France)	v	--	--	identified vivianite subspectra and other probable major contributors such as poorly formed ferrihydrite, goethite, and hematite	24A007
Rh(IS/ $\alpha$ -Fe)	pristine and milled BaTi <sub>0.90</sub> Fe <sub>0.10</sub> O <sub>3-<math>\delta</math></sub>	300	--	--	observed three kinds of components: one or two ferromagnetic, antiferromagnetic and paramagnetic	24B011
Rh(IS/ $\alpha$ -Fe)	product of electrochemical oxidation treatment of oilfield wastewater	298	0.168	0	identified the generation of Na <sub>2</sub> FeO <sub>3</sub> in an anodic oxidation system	24G007
xx(IS/ $\alpha$ -Fe)	pure Na <sub>2</sub> Fe <sub>0.5</sub> Mn <sub>0.5</sub> PO <sub>4</sub> F and dopamine-coated Na <sub>2</sub> Fe <sub>0.5</sub> Mn <sub>0.5</sub> PO <sub>4</sub> F	v	--	--	identified both Fe(II) and Fe(III) before coating and only Fe(II) after coating	24E001
Rh(IS/ $\alpha$ -Fe)	soil from the Mulde river floodplain near Muldenstein (Germany) amended with 0, 10, and 50 g/kg straw	v	--	--	identified mononuclear organic Fe(III) complexes, Fe(III) in low-Fe silicates, silicate-bound Fe(II), Fe(III) oxyhydroxides, ferrihydrite and hematite	24M003
Rh(IS/ $\alpha$ -Fe)	tetragonal CuFe <sub>2</sub> O <sub>4</sub> nanoparticles	300	--	--	identified sextets of hematite impurity and Fe(III) cations on B-sites and tetrahedral A-sites with approximate equal occupancy	24J004
Rh(IS/ $\alpha$ -Fe)	ultrafine two-line-ferrihydrite nanoparticles with varying magnetic interparticle interactions strength tuned by coating	v	--	--	determined the relaxation times to compare with the data determined by static and dynamic magnetic susceptibilities	24B013
Rh(IS/ $\alpha$ -Fe)	$\delta$ -FeOOH nanosheets	14	--	--	identified abundant 5-coordinated iron sites in $\delta$ -FeOOH and confirmed the iron-peroxy species	24K009
<u>Fe-57 14.40 keV Transition: Inorganic Sulfides</u>						
Rh(IS/ $\alpha$ -Fe)	airborne particulate matter in the lichen Punctelia hypoleucites (Argentina)	v	--	--	determined the presence of pyrite (FeS <sub>2</sub> ) and ferrous sulfate particles	24H007
Rh(IS/ $\alpha$ -Fe)	Fe <sub>0.05</sub> TiS <sub>2-<math>\delta</math></sub>	300	0.731	0.440	Fe atoms are surrounded octahedrally by S atoms	24D006
<u>Fe-57 14.40 keV Transition: Inorganic Sulphates</u>						
Rh(IS/ $\alpha$ -Fe)	airborne particulate matter in the lichen Punctelia hypoleucites (Argentina)	v	--	--	determined the presence of pyrite (FeS <sub>2</sub> ) and ferrous sulfate particles	24H007
Rh(IS/ $\alpha$ -Fe)	product of electrochemical oxidation treatment of oilfield wastewater	298	0.168	0	identified the generation of Na <sub>2</sub> FeO <sub>3</sub> in an anodic oxidation system	24G007



Source	Absorber	Temp	IS	QS	Comments	Code
<u>Fe-57 14.40 keV Transition: Irradiation Experiments</u>						
Rh(IS/ $\alpha$ -Fe)	'as received' and 'neutron irradiated' 50 $\mu$ m Fe-Cr alloy	v	--	--	identified an increase of mean hyperfine field ascribed to phase separation of Fe/Cr/Al fractions	24D012
Rh(IS/ $\alpha$ -Fe)	Fenton catalysts UiO-66-NH <sub>2</sub> -(Zr/Fe) nanoparticles unsupported and supported on the graphene aerogel substrate	300	--	--	the supported catalysts exhibit a larger quadrupole splitting (QS) (0.662mm·s <sup>-1</sup> ) compared to unsupported (QS = 0.584mm·s <sup>-1</sup> ); the increased QS is attributed to a more distorted site	24Z003
Rh(IS/ $\alpha$ -Fe)	ferritic-martensitic steels EP823 and EP823-ODS before and after neutron irradiation at 505 °C to a dose of 85 dpa without and with quasi-hydrostatic stress	v	--	--	determined the P(H) distributions with <sup>57</sup> Fe atom components distinguished by Cr entered the <sup>57</sup> Fe environment for two nearest coordination shells	24K013
<u>Fe-57 14.40 keV Transition: Metals and Alloys</u>						
Rh(IS/ $\alpha$ -Fe)	'as received' and 'neutron irradiated' 50 $\mu$ m Fe-Cr alloy	v	--	--	identified an increase of mean hyperfine field ascribed to phase separation of Fe/Cr/Al fractions	24D012
Rh(IS/ $\alpha$ -Fe)	core/shell FeRh@FeO nanoparticles	v	--	--	identified both magnetic and spm-components in both alloys and iron oxides or/and iron oxyhydroxides phases	24K008
Rh(IS/ $\alpha$ -Fe)	Fe <sub>1-x</sub> Co <sub>x</sub> Si ( $x \geq 0.3$ ) with B <sub>20</sub> -type crystal structure	v	--	--	observed doping-driven magnetic phase transition point occurs around $x = 0.7$ , accompanied by non-Fermi-liquid behaviors at low temperatures	24H006
xx(IS/ $\alpha$ -Fe)	Fe <sub>82-x</sub> B <sub>10</sub> P <sub>7.5</sub> Cu <sub>0.5</sub> Nb <sub>x</sub> ( $x = 0, 0.5, 1.0, \& 1.5$ ) alloy ribbons	v	--	--	identified a broadened sextet with enhanced lines 2 and 5 suggesting a preferred orientation of easy magnetization axis	24L003
Rh(IS/ $\alpha$ -Fe)	ferritic-martensitic steels EP823 and EP823-ODS before and after neutron irradiation at 505 °C to a dose of 85 dpa without and with quasi-hydrostatic stress	v	--	--	determined the P(H) distributions with <sup>57</sup> Fe atom components distinguished by Cr entered the <sup>57</sup> Fe environment for two nearest coordination shells	24K013
Rh(IS/ $\alpha$ -Fe)	high-chromium ferritic-martensitic steel NS <sub>219</sub>	300	--	--	measured the dependence of the relative area of 11 sextets, especially P(0,0), and a singlet as a function of time while annealing a temperature of 475 °C	24K004
Rh(IS/ $\alpha$ -Fe)	high-entropy alloy Fe <sub>20</sub> Co <sub>20</sub> Ni <sub>20</sub> Al <sub>20</sub> Mn <sub>20</sub>	300	--	--	identified 2 six-line distributions assigned to 1NN and 2NN environments and a minor (2.5%) singlet	24K010
Rh(IS/ $\alpha$ -Fe)	iron meteorites Anyujskij IIAB and Gibeon IVA, stony-iron meteorite Seymchan PMG and stony meteorites Annama H <sub>5</sub> and Kemer L4	295	--	--	determined Fe hyperfine parameters in the phases $\alpha$ -Fe(Ni, Co), $\alpha$ -Fe(Ni, Co), $\gamma$ -Fe(Ni, Co) and $\gamma$ -FeNi(Co)	24G005
Rh(IS/ $\alpha$ -Fe)	iron single atoms in graphene structures	300	--	--	detected the total amount of Fe atoms intercalated between graphene layers at the level of 1.3 ppm	24K012
Rh(IS/ $\alpha$ -Fe)	Jilin meteorite	300	--	--	sample thickness in ordinary chondrite has no effect on percentages of Mössbauer spectral areas of troilite and FeNi alloy (kamacite and taenite) and olivine and pyroxene	24J003
Rh(IS/ $\alpha$ -Fe)	nanocrystalline ferromagnetic Fe-Cu-Nb-Si-B microwires	298	--	--	observed two kinds of components: a ferromagnetic related to the distribution of hyperfine fields for amorphous phase, and other one is the discrete subspectra components for nanograins with narrow sextet lines	24H005
Rh(IS/ $\alpha$ -Fe)	Nd <sub>0.2</sub> Tb <sub>0.3</sub> Dy <sub>0.5</sub> Fe <sub>1.93</sub> and Nd <sub>0.2</sub> Tb <sub>0.3</sub> Dy <sub>0.5</sub> Fe <sub>1.93</sub> /epoxy composites	300	--	--	identified <111> as the easy magnetic direction from the intensity ratio 3:1 of two sextets	24D005
Rh(IS/ $\alpha$ -Fe)	parent alloy Zr <sub>4</sub> Fe <sub>2</sub> O <sub>0.6</sub> and saturated deuterides Zr <sub>4</sub> Fe <sub>2</sub> O <sub>0.25</sub> D <sub>9.9</sub> and Zr <sub>4</sub> Fe <sub>2</sub> O <sub>0.6</sub> D <sub>7.5</sub>	v	--	--	identified at 4.2 K broadened doublets for the parent compound and both doublets and sextets in hydrides; their coexistence is attributed to Zr/Fe disorder	24Z004
Rh(IS/ $\alpha$ -Fe)	Sm <sub>2</sub> (Fe <sub>1-x</sub> Mn <sub>x</sub> ) <sub>14</sub> B ( $0 \leq x \leq 0.3$ )	v	--	--	identified magnetic sextets and partially or fully collapsed spectral signatures of the sites 16k <sub>1</sub> , 16k <sub>2</sub> , 8j <sub>1</sub> , 8j <sub>2</sub> , 4c, 4e	24Y001
Rh(IS/ $\alpha$ -Fe)	ternary alloys Fe <sub>0.90</sub> Cr <sub>0.05</sub> Si <sub>0.05</sub> and Fe <sub>0.85</sub> Cr <sub>0.10</sub> Si <sub>0.05</sub> prepared by mechanical alloying before and after several anneals in vacuum and in air	300	--	--	observed phases of bcc alloys, and Fe <sub>2</sub> O <sub>3</sub> and Fe <sub>3</sub> O <sub>4</sub> , induced by annealing in air	23S097
TmB <sub>12</sub>	Yb <sub>3</sub> Cu <sub>4</sub> Ge <sub>4</sub>	v	--	--	reviewed paramagnetic and Zeeman-split spectra and magnetic behavior of Yb <sub>3</sub> Cu <sub>4</sub> Ge <sub>4</sub> and Gd <sub>3</sub> Cu <sub>4</sub> Ge <sub>4</sub> and hyperfine parameters in many other intermetallic ytterbium compounds	24E002
<u>Fe-57 14.40 keV Transition: Miscellaneous Experiments</u>						
xx(IS/ $\alpha$ -Fe)	Fe <sub>82-x</sub> B <sub>10</sub> P <sub>7.5</sub> Cu <sub>0.5</sub> Nb <sub>x</sub> ( $x = 0, 0.5, 1.0, \& 1.5$ ) alloy ribbons	v	--	--	identified a broadened sextet with enhanced lines 2 and 5 suggesting a preferred orientation of easy magnetization axis	24L003

Source	Absorber	Temp	IS	QS	Comments	Code
Rh(IS/ $\alpha$ -Fe)	Fenton catalysts UiO-66-NH <sub>2</sub> -(Zr/Fe) nanoparticles unsupported and supported on the graphene aerogel substrate	300	--	--	the supported catalysts exhibit a larger quadrupole splitting (QS) (0.662mm·s <sup>-1</sup> ) compared to unsupported (QS=0.584mm·s <sup>-1</sup> ); the increased QS is attributed to a more distorted site	24Z003
Rh(IS/ $\alpha$ -Fe)	initial iron powder and nano-iron-biochar and their corrosion products after one month of humidity exposure in cellulose and in peat	v	--	--	identified alpha and gamma iron, alpha and gamma FeOOH and theta-Fe <sub>3</sub> C	24P001
Rh(IS/ $\alpha$ -Fe)	iron single atoms in graphene structures	300	--	--	detected the total amount of Fe atoms intercalated between graphene layers at the level of 1.3 ppm	24K012
xx(IS/ $\alpha$ -Fe)	pure Na <sub>2</sub> Fe <sub>0.5</sub> Mn <sub>0.5</sub> PO <sub>4</sub> F and dopamine-coated Na <sub>2</sub> Fe <sub>0.5</sub> Mn <sub>0.5</sub> PO <sub>4</sub> F	v	--	--	identified both Fe(II) and Fe(III) before coating and only Fe(II) after coating	24E001
Rh(IS/ $\alpha$ -Fe)	{[Fe(Tp)(CN) <sub>3</sub> ] <sub>2</sub> [Fe(bnbpen)] <sub>2</sub> }(ClO <sub>4</sub> ) <sub>2</sub> ·8CH <sub>3</sub> OH (bnbpen = N,N-bis-(2-naphthylmethyl)-N, N-bis(2-picolayl)-ethylenediam ine)	v	--	--	identified both Fe(II)LS and Fe(II)HS and Fe(III) components and observed a thermal ETCST process involving the transformation of {Fe <sup>III</sup> ,LS( $\mu$ -CN)Fe <sup>II</sup> ,HS} <sub>2</sub> (HT phase) and {Fe <sup>II</sup> ,LS( $\mu$ -CN)Fe <sup>III</sup> ,LS} <sub>2</sub> (LT phase)	24J002
<b>Fe-57 14.40 keV Transition: Miscellaneous Inorganic Compounds</b>						
Rh(IS/ $\alpha$ -Fe)	airborne particulate matter in the lichen Punctelia hypoleucites (Argentina)	v	--	--	determined the presence of pyrite (FeS <sub>2</sub> ) and ferrous sulfate particles	24H007
Rh(IS/ $\alpha$ -Fe)	Biogenic iron oxide particles alone and supported on montmorillonite (BioFe and BioFe-MMT)	300	--	--	identified several Fe <sup>3+</sup> and Fe <sup>2+</sup> subspectra and determined the relative abundances of Fe <sup>2+</sup> and Fe <sup>3+</sup>	24P002
Rh(IS/ $\alpha$ -Fe)	coprecipitated catalysts Fe-cp, FeZn-cp, and FeZn-2.8Na before and after 100 h FT reaction	300	--	--	identified in the spent catalysts the phases of Fe <sub>3</sub> O <sub>4</sub> , Fe <sub>5</sub> C <sub>2</sub> , Fe <sub>7</sub> C <sub>3</sub> , and spm-Fe <sup>3+</sup>	24G003
Rh(IS/ $\alpha$ -Fe)	double metal oxalates MM'(C <sub>2</sub> O <sub>4</sub> ) <sub>2</sub> ·4H <sub>2</sub> O (M=Fe, M'= Mg, Co, Zn) and triple metal oxalates MM'M''(C <sub>2</sub> O <sub>4</sub> ) <sub>3</sub> ·6H <sub>2</sub> O (M=Fe, M'=Mg, Mn, Co; M''= Zn)	298	1.195	1.72	identified an asymmetric doublet that assigned to Fe <sup>2+</sup> in octahedral sites with the asymmetry assigned to texture effects	24M005
xx(IS/ $\alpha$ -Fe)	Fe <sub>82-3</sub> B <sub>10</sub> P <sub>7.5</sub> Cu <sub>0.5</sub> Nb <sub>x</sub> (x= 0, 0.5, 1.0, & 1.5) alloy ribbons	v	--	--	identified a broadened sextet with enhanced lines 2 and 5 suggesting a preferred orientation of easy magnetization axis	24L003
Rh(IS/ $\alpha$ -Fe)	Fenton catalysts UiO-66-NH <sub>2</sub> -(Zr/Fe) nanoparticles unsupported and supported on the graphene aerogel substrate	300	--	--	the supported catalysts exhibit a larger quadrupole splitting (QS) (0.662mm·s <sup>-1</sup> ) compared to unsupported (QS=0.584mm·s <sup>-1</sup> ); the increased QS is attributed to a more distorted site	24Z003
Rh(IS/ $\alpha$ -Fe)	glass-crystalline materials in the system Na <sub>2</sub> O/CaO/SiO <sub>2</sub> /Fe <sub>2</sub> O <sub>3</sub> with the Fe <sub>2</sub> O <sub>3</sub> concentrations of 20, 25 and 30 mol%	300	--	--	identified doublets of Fe <sup>3+</sup> and Fe <sup>2+</sup> and up to 7 sextets assigned to epsilon-Fe <sub>2</sub> O <sub>3</sub> and spinel phases	24H008
Rh(IS/ $\alpha$ -Fe)	initial iron powder and nano-iron-biochar and their corrosion products after one month of humidity exposure in cellulose and in peat	v	--	--	identified alpha and gamma iron, alpha and gamma FeOOH and theta-Fe <sub>3</sub> C	24P001
Rh(IS/ $\alpha$ -Fe)	InNi <sub>3</sub> C <sub>0.5</sub> /Fe <sub>3</sub> O <sub>4</sub> catalyst	v	--	--	identified A and B sextets of Fe <sub>3</sub> O <sub>4</sub>	24M002
Rh(IS/ $\alpha$ -Fe)	iron single atoms in graphene structures	300	--	--	detected the total amount of Fe atoms intercalated between graphene layers at the level of 1.3 ppm	24K012
Rh(IS/ $\alpha$ -Fe)	layered carbosilicate formed from CNT with up to 10 wt% iron content (10Fe-CSiO <sub>x</sub> ) compared to iron silicate without carbon	80	--	--	identified 85% of Fe <sup>3+</sup> and 15% of Fe <sup>2+</sup> in 10Fe-CSiO <sub>x</sub> , while 100% of Fe <sup>3+</sup> in iron silicate without carbon	24D011
Rh(IS/ $\alpha$ -Fe)	nanocrystalline ferromagnetic Fe-Cu-Nb-Si-B microwires	298	--	--	observed two kinds of components: a ferromagnetic related to the distribution of hyperfine fields for amorphous phase, and other one is the discrete subspectra components for nanograins with narrow sextet lines	24H005

Source	Absorber	Temp	IS	QS	Comments	Code
Rh(IS/ $\alpha$ -Fe)	parent alloy $Zr_4Fe_2O_{0.6}$ and saturated deuterides $Zr_4Fe_2O_{0.25}D_{9.9}$ and $Zr_4Fe_2O_{0.6}D_{7.5}$	v	--	--	identified at 4.2 K broadened doublets for the parent compound and both doublets and sextets in hydrides; their coexistence is attributed to Zr/Fe disorder	24Z004
xx(IS/ $\alpha$ -Fe)	pure $Na_2Fe_{0.5}Mn_{0.5}PO_4F$ and dopamine-coated $Na_2Fe_{0.5}Mn_{0.5}PO_4F$	v	--	--	identified both Fe(II) and Fe(III) before coating and only Fe(II) after coating	24E001
Rh(IS/ $\alpha$ -Fe)	soil profile samples collected from Salcedo Experimental Station of Institute of Agrarian Innovation	293	--	--	identified the doublet contributions of cis- $Fe^{3+}$ and trans- $Fe^{3+}$ and edge- $Fe^{2+}$ in clay and magnetic phases of hematite and goethite	24M006
Rh(IS/ $\alpha$ -Fe)	$\{[Fe(Tp)(CN)_2][Fe(bnbpen)]_2(CIO_4)_2 \cdot 8CH_3OH$ (bnbpen = N,N-bis-(2-naphthylmethyl)-N, N'-bis(2-picolyl)-ethylenediamine)	v	--	--	identified both Fe(II)LS and Fe(II)HS and Fe(III) components and observed a thermal ETCST process involving the transformation of $\{Fe^{III}LS(\mu-CN)Fe^{II}HS\}_2$ (HT phase) and $\{Fe^{II}LS(\mu-CN)Fe^{III}LS\}_2$ (LT phase)	24J002
<u>Fe-57 14.40 keV Transition: Organic Compounds</u>						
Rh(IS/ $\alpha$ -Fe)	$(HNEt_3)[FeL_3] \cdot 0.5H_2O$ with HL = 4,6-di-tert-butyl-1,2-benzoquinone-2-monooxime	14	0.17	1.06	identified a doublet assigned to ferrous iron in a low spin state	24K006
Rh(IS/ $\alpha$ -Fe)	composite of $[Fe(atrz)_3]Cl_{1.5}(BF_4)_{0.5}$ in polystyrene	293	--	--	identified the LS and HS spin state distribution after the implementation of the complex into the polymer	24K003
Rh(IS/ $\alpha$ -Fe)	double metal oxalates $MM'(C_2O_4)_2 \cdot 4H_2O$ (M=Fe, M'=Mg, Co, Zn) and triple metal oxalates $MM'M''(C_2O_4)_3 \cdot 6H_2O$ (M=Fe, M'=Mg, Mn, Co; M''=Zn)	298	1.195	1.72	identified an asymmetric doublet that assigned to $Fe^{2+}$ in octahedral sites with the asymmetry assigned to texture effects	24M005
Rh(IS/ $\alpha$ -Fe)	heteroleptic amine complex $[Fe(en)(tren)][FeSe_2]_2$ (en=ethylenediamine, $C_2H_8N_2$ , tren=tris(2-aminoethyl)amine, $C_6H_{18}N_4$ )	v	--	--	identified components with the ratio between the intensities approximately 2:1, and confirmed the separation of $Fe^{3+}$ and $Fe^{2+}$ sublattices	24G009
Rh(IS/ $\alpha$ -Fe)	Hexakis(urea)iron(III) complexes with different anions ( $X=Cl^-$ , $Br^-$ , $ClO_4^-$ , $NO_3^-$ , $MnO_4^-$ , $(S_2O_8)^{2-}$ )	v	--	--	identified a broadened Lorentzian singlet (paramagnetic spin relaxation line shape), assigned to HS $Fe^{3+}$	24B012
Rh(IS/ $\alpha$ -Fe)	iron(III) citrate frozen solutions at different Fe to citrate molar ratios	5	--	--	confirmed the coexistence of several monoiron species with different coordination environments	24G001
Rh(IS/ $\alpha$ -Fe)	mononuclear benzoylformate complex, $[Fe(Im^{Ph2}NNO^{tBu})(BF)]$	80	1.17	2.64	identified N,N,O-bound iron(II) pentacoordinate site, similar to $O_2$ -reactive active sites of $\alpha$ KG-dependent iron enzymes	24M008
Rh(IS/ $\alpha$ -Fe)	polyacrylonitrile- $[Fe(atrz)_3](2ns)_2$ -foil	293	0.440	0.185	identified the LS spin state of Fe(II)	24K003
Rh(IS/ $\alpha$ -Fe)	soil from the Mulde river floodplain near Muldenstein (Germany) amended with 0, 10, and 50 g/kg straw	v	--	--	identified mononuclear organic Fe(III) complexes, Fe(III) in low-Fe silicates, silicate-bound Fe(II), Fe(III) oxyhydroxides, ferrihydrite and hematite	24M003
Rh(IS/ $\alpha$ -Fe)	soil profile samples collected from Salcedo Experimental Station of Institute of Agrarian Innovation	293	--	--	identified the doublet contributions of cis- $Fe^{3+}$ and trans- $Fe^{3+}$ and edge- $Fe^{2+}$ in clay and magnetic phases of hematite and goethite	24M006
Rh(IS/ $\alpha$ -Fe)	trinuclear cyanido-bridged complexes	v	--	--	identified Fe(II) LS and Fe(II) HS in two structure sites	24H004
Rh(IS/ $\alpha$ -Fe)	$[^{57}Fe^{III}(O)Mn^{II}poat]^+$ in PrCN and $[^{57}Fe^{III}(O)Mn^{IV}poat]^{2+}$ in PrCN	4.2	--	--	first quantitative demonstration of the effect of the hyperfine interaction from a non-Fe nucleus on the Mössbauer spectra	24L004
Rh(IS/ $\alpha$ -Fe)	$[Fe(atrz)_3](2ns)_2$	293	0.278	0.074	identified the LS spin state of Fe(II)	24K003
<u>Fe-57 14.40 keV Transition: Terrestrial and Extraterrestrial Minerals</u>						
Rh(IS/ $\alpha$ -Fe)	Biogenic iron oxide particles alone and supported on montmorillonite (BioFe and BioFe-MMT)	300	--	--	identified several $Fe^{3+}$ and $Fe^{2+}$ subspectra and determined the relative abundances of $Fe^{2+}$ and $Fe^{3+}$	24P002
Rh(IS/ $\alpha$ -Fe)	borosilicate waste glasses synthesized under a variety of redox conditions	300	--	--	measured $Fe^{2+}/Fe(\text{total})$ ratio to compare with XANES data	24M007

Source	Absorber	Temp	IS	QS	Comments	Code
Rh(IS/ $\alpha$ -Fe)	collected from the different weathering zones andesitic pumice: greyish weathered pumice (GP), white weathered pumice (WP), and brownish weathered pumice of Lake Shikotsu	v	--	--	determined the relative abundances of Fe <sup>2+</sup> and Fe <sup>3+</sup>	24F003
Rh(IS/ $\alpha$ -Fe)	Fe-doped kaolinite	300	--	--	identified a doublet of Fe(II) and two doublets of Fe(III) : 6-coordination Fe(III) and 4-coordination Fe(III)	24C005
Rh(IS/ $\alpha$ -Fe)	initial iron powder and nano-iron-biochar and their corrosion products after one month of humidity exposure in cellulose and in peat	v	--	--	identified alpha and gamma iron, alpha and gamma FeOOH and theta-Fe <sub>3</sub> C	24P001
Rh(IS/ $\alpha$ -Fe)	iron meteorites Anyujskij IIAB and Gibeon IVA, stony-iron meteorite Seymchan PMG and stony meteorites Annama H <sub>5</sub> and Kemer L4	295	--	--	determined Fe hyperfine parameters in the phases $\alpha$ -Fe(Ni, Co), $\alpha$ -Fe(Ni, Co), $\gamma$ -Fe(Ni, Co) and $\gamma$ -FeNi(Co)	24G005
Rh(IS/ $\alpha$ -Fe)	isocubanite from seafloor hydrothermal deposits in the Okinawa Trough before and after heating	v	--	--	identified sites 1 and 2 of CuFe <sub>3</sub> S <sub>4</sub> and chalcopyrite	24K002
Rh(IS/ $\alpha$ -Fe)	Jilin meteorite	300	--	--	sample thickness in ordinary chondrite has no effect on percentages of Mössbauer spectral areas of troilite and FeNi alloy (kamacite and taenite) and olivine and pyroxene	24J003
Rh(IS/ $\alpha$ -Fe)	Loess-soil from the Terek-Kuma lowland	v	--	--	identified goethite and hematite and several doublets assigned to Fe <sup>2+</sup> and Fe <sup>3+</sup> and determined the ratio of Fe <sup>2+</sup> /(Fe <sup>3+</sup> + Fe <sup>2+</sup> )	24A006
Rh(IS/ $\alpha$ -Fe)	product of electrochemical oxidation treatment of oilfield wastewater	298	0.168	0	identified the generation of Na <sub>2</sub> FeO <sub>3</sub> in an anodic oxidation system	24G007
Rh(IS/ $\alpha$ -Fe)	soil from the Mulde river floodplain near Muldenstein (Germany) amended with 0, 10, and 50 g/kg straw	v	--	--	identified mononuclear organic Fe(III) complexes, Fe(III) in low-Fe silicates, silicate-bound Fe(II), Fe(III) oxyhydroxides, ferrihydrite and hematite	24M003
Rh(IS/ $\alpha$ -Fe)	soil profile samples collected from Salcedo Experimental Station of Institute of Agrarian Innovation	293	--	--	identified the doublet contributions of cis-Fe <sup>3+</sup> and trans-Fe <sup>3+</sup> and edge-Fe <sup>2+</sup> in clay and magnetic phases of hematite and goethite	24M006
<u>Sn-119 23.80 keV Transition: FERROMAGNETIC</u>						
Ca <sup>119m</sup> SnO <sub>3</sub>	Heusler alloys Rh <sub>2</sub> Mn <sub>1+x</sub> Sn <sub>1-x</sub> (0 ≤ x ≤ 0.6)	v	--	--	the values of supertransferred B <sub>hf</sub> at 90 K increase with increasing x, while at 293 K decrease linearly with increasing x	24A011
<u>Sn-119 23.80 keV Transition: Inorganic Oxides</u>						
CaSnO <sub>3</sub> (IS/BaSnO <sub>3</sub> )	nanoparticles of $\alpha$ -FeOOH, $\alpha$ -Sn <sub>0.10</sub> Fe <sub>0.90</sub> OOH, $\alpha$ -Sn <sub>0.15</sub> Fe <sub>0.85</sub> OOH, and $\alpha$ -Sn <sub>0.2</sub> Fe <sub>0.8</sub> OOH	v	--	--	identified the increasing values of $\delta$ from 0.02 to 0.08 mm s <sup>-1</sup> assigned to increased covalence of the chemical bond between the Sn <sup>IV</sup> -O <sup>2-</sup>	24I005
<u>Sn-119 23.80 keV Transition: Metals and Alloys</u>						
Ca <sup>119m</sup> SnO <sub>3</sub>	Heusler alloys Rh <sub>2</sub> Mn <sub>1+x</sub> Sn <sub>1-x</sub> (0 ≤ x ≤ 0.6)	v	--	--	the values of supertransferred B <sub>hf</sub> at 90 K increase with increasing x, while at 293 K decrease linearly with increasing x	24A011
CaSnO <sub>3</sub>	Ni-Mn-based Heusler compound Ni <sub>2</sub> MnSn	300	--	--	observed four sextets instead of expected one in ordered L2 <sub>1</sub> structure, and interpreted them as caused by thermal anti-site disorder leading to a swap of different kinds of atoms	24F001
<u>Yb-171 66.70 keV Transition</u>						
Rh(IS/ $\alpha$ -Fe)	Na <sub>1-x</sub> Fe <sub>1-y</sub> Ni <sub>y</sub> O <sub>2</sub> cathodes	v	--	--	reviewed the Mössbauer spectroscopy studies indicating a partial oxidation of iron ions (i.e., Fe <sup>3+</sup> to Fe <sup>4+</sup> ) during charging	24O003
<u>Zn-67 93.30 keV Transition</u>						
CuCl	ZnS	300	--	--	QS of impurity zinc centers in sodium halides are consistent with the QS values calculated within the framework of the ionic model.	23M059
CuI	ZnS	300	--	--	QS of impurity zinc centers in sodium halides are consistent with the QS values calculated within the framework of the ionic model.	23M059
NaCl	ZnS	300	--	--	QS of impurity zinc centers in sodium halides are consistent with the QS values calculated within the framework of the ionic model	23M059
NaI	ZnS	300	--	--	QS of impurity zinc centers in sodium halides are consistent with the QS values calculated within the framework of the ionic model	23M059

Actinides: 24E002				Computer Programs: 23O012 24A008				Glasses and Amorphous Substances: 24A005 24H005 24K011 24L003 24M007 24Z003	
Analysis: 23O012 24J003 24K013				Crystal Defects: 22M052 23H037 23M059 23S097 24C004 24D012 24F001 24G004 24K005 24Z004				Glazes: 24H008	
Anti-ferromagnetism: 23S094 24B010 24B011 24B013 24C004 24E002 24G009 24G010 24H004 24I003 24I004 24L005 24L006 24R001 24T003				Crystal Field Theory: 22M052 24E002 24G002				Hartree-Fock Calculations: 22M052 23H037 24A008 24C005 24D008 24F001 24G002 24K009 24M008 24O003 24Y001	
Applied Electric Field: 23H037 24D007 24D008 24E001 24O003				Curie Temperature: 24A011 24E002 24T003 24Y001				High Pressure Experiments: 23Y024 24K013 24L005	
Applied Magnetic Field: 22M052 24G001 24G006 24G009 24I003 24K005 24L005 24R001 24T003				Debye Temperature: 24B014 24I005				Inorganic Cyanides: 24H004 24J002 24L004 24M008	
Asymmetry Parameter: 23M059 24G001 24H006 24L004 24R001				Decomposition: 23S097 24F002 24G003 24P002				Inorganic Halides: 23M059	
Bacteria: 24A007 24B013 24G006 24L004 24P002				Delayed Time Experiments: 23H037				Instrumentation: 23O012 24L003	
Biological Applications: 24A007 24A008 24B013 24F003 24G006 24H007 24K009 24L004 24M009 24P001 24P002				Detectors: 22M052				Intercalation Compounds: 24C005 24D006 24I005 24K012	
Carbonyl Complexes: 24D007 24G003 24M005 24P001				Diffusion: 24K004				Ion Implantation: 22M052	
Catalysts: 23H037 24D007 24D008 24E001 24F002 24G002 24G003 24G004 24K009 24L007 24M002 24M008 24M009 24Z003				Distributions of Magnetic Fields: 23S094 23S097 23Y024 24A006 24A007 24A009 24A010 24A011 24B010 24B011 24B013 24B014 24C004 24D009 24D010 24D012 24F002 24G003 24G004 24G005 24G006 24G007 24G008 24G009 24H005 24H006 24H007 24H008 24I003 24I005 24J003 24J004 24K002 24K004 24K005 24K007 24K008 24K009 24K010 24K013 24L003 24L004 24L006 24L007 24M002 24M003 24M004 24M006 24M009 24P001 24R001 24Y001 24Z004				Irradiation Experiments: 22M052 24D012 24K013 24Z003	
Cement: 24L008				Electron Diffraction: 23Y024 24B014 24D005 24D007 24D010 24F002 24G003 24G004 24G008 24L003 24L008 24P001 24P002 24Z003				Jahn-Teller Effect: 24B010 24L006 24O003	
Charge States: 22M052 24A007 24D007 24D008 24E001 24F002 24G002 24G003 24G004 24G009 24H008 24I005 24J002 24M002 24M003 24M008 24O003 24P002 24T003 24Z003				Electron Microscopy: 23S097 23Y024 24A007 24B010 24B012 24B014 24D005 24D006 24D007 24D011 24E001 24F002 24G003 24G004 24G005 24G008 24H007 24H008 24I003 24J004 24K002 24K004 24K005 24K007 24K008 24K009 24K013 24L003 24L007 24L008 24M002 24M009 24P001 24P002 24Y001 24Z003				Kinetics: 23Y024 24A006 24E001 24F002 24G004 24G007 24K002 24K004 24L007 24M002 24M003 24O003 24Z003	
Charge Transfer: 23H037 24A007 24D007 24D008 24D009 24F002 24G007 24I005 24J002 24J004 24L004 24L007 24M008 24O003 24Z003				Electron Paramagnetic Resonance: 24B012 24B013 24D008 24E002 24G001 24G006 24K003 24K009 24M008 24Z003				Lattice Dynamics: 24A008 24A010 24B014 24D009 24D010 24F001 24G002 24K007 24M004 24Z004	
Chemical Identification: 22M052 23H037 23M059 23S094 23S097 23Y024 24A006 24A007 24A008 24A009 24A010 24A011 24B010 24B013 24B014 24C004 24C005 24D005 24D006 24D007 24D008 24D009 24D010 24D011 24F001 24F002 24F003 24G001 24G003 24G004 24G005 24G006 24G007 24G008 24G010 24H003 24H004 24H005 24H006 24H007 24H008 24I004 24I005 24J002 24J004 24K004 24K007 24K009 24K010 24K012 24K013 24L004 24L007 24L008 24M004 24M007 24M009 24O003 24P002 24T003				Electronic Spectroscopy: 23H037 23S097 24A008 24A010 24B010 24B011 24B012 24B014 24D006 24D007 24D008 24D009 24D010 24D011 24D012 24E002 24G002 24G003 24G004 24G007 24K003 24K004 24K007 24K011 24L004 24L006 24M002 24M008 24O003 24P002				Mass Spectroscopy: 24Z003	
Chemical Kinetics: 23H037 24D008 24F002 24G007 24L007 24Z003				Ferromagnetic Materials: 24A011 24B011 24B013 24C004 24D010 24E002 24G009 24H005 24I003 24I004 24K007 24L005 24L006 24T003 24Y001				Matrix Isolation: 24K012	
Chemical Reactions: 23H037 23S097 23Y024 24A008 24B012 24C005 24D007 24D008 24D009 24D011 24F002 24F003 24G003 24G007 24G009 24H008 24J004 24K004 24K006 24K009 24L007 24L008 24M002 24M003 24M008 24M009 24P002 24Z003				Fraction of Zero Phonons-Absorber: 24J003				Mechanical Milling: 23S097 24B011	
Clay Minerals: 24C005 24F003 24M006 24P002				Fraction of Zero Phonons-Source: 24J003				Metals and Alloys: 23S097 24A011 24D005 24D012 24E002 24F001 24G005 24H005 24H006 24J003 24K004 24K008 24K010 24K012 24K013 24L003 24R001 24Y001 24Z004	
				Frozen Solutions: 24G001				Meteorites: 24G005 24J003	
								Minicomputer Interfacing: 23O012	
								Molecular Orbital Calculations: 24A008 24C005 24G002	
								Nanocrystal: 23Y024 24B013 24B014 24D007 24D009 24D010 24G004 24G008 24H005 24I003 24I004 24K005 24K007 24K008 24L008 24M009 24P001 24Z003	
								Neel Temperature: 23S094 24B010 24E002 24H004 24L006 24R001 24T003	
								Neutron Diffraction: 24R001	
								Nuclear Forward Scattering: 23H037	

Nuclear Magnetic Resonance Experiments:				Sediments:				Synchrotron Radiation:			
24E002	24G006	24M008		24A007	24F003			23H037	24A008		
Phase Transitions:				Semiconductors:				Terrestrial and Extrater. Minerals:			
24E002	24G004	24J002	24K003	24D009	24K011			24A006	24C005	24F003	24G005
24K004	24R001	24T003	24Y001	Single Crystal Experiments:				24G007	24J003	24K002	24M003
Polymers:				22M052	24A008	24I003		24M006	24M007	24P001	24P002
23Y024	24B012	24F002	24G004	Soil:				Texture:			
24G009	24K003			24A006	24M003	24M006	24P001	22M052	24D005	24D011	24H005
Quantitative Analysis:				Source Experiments:				24K012	24K013	24L003	24L008
24C005	24F003	24K011	24K012	22M052	23M059			24M005	24M006	24P002	24Z003
24K013				Source Preparation:				Theory:			
Radiation Damage - Nuclear Reactors:				22M052	23M059			23M059	24A008	24E002	24K006
24D012	24K013			Spectrometers:				24K010	24Y001		
Raman Spectroscopy:				23O012				Thin Films:			
24A008	24B012	24D008	24D009	Spin Crossover:				22M052	24G004		
24D010	24E001	24K007	24K009	24H004	24J002	24K003		Variable Thickness:			
24M004								22M052	24J003		
Rare Earths:				Steel:				X-ray Diffraction-Powder:			
24B010	24D005	24E002	24G008	24K004	24K013			23S094	23Y024	24A005	24A006
24G010	24H003	24K011	24L004	Strain Effects:				24A007	24A008	24A009	24A010
24L006	24M004	24M007	24R001	24D005	24G010	24K013		24B010	24B013	24B014	24C004
24T003	24Y001			Superconductivity:				24C005	24D005	24D006	24D007
Relaxation:				24E002	24T003			24D008	24D009	24D010	24D011
24A009	24A010	24B010	24B012	Superparamagnetism:				24E001	24F002	24F003	24G001
24B013	24C004	24D007	24D009	24A009	24A010	24B010	24B013	24G003	24G004	24G005	24G006
24D010	24F003	24G003	24H007	24C004	24D007	24D009	24D010	24G007	24G008	24G009	24H003
24I003	24I005	24K005	24K007	24F003	24G003	24H007	24I003	24H004	24H005	24H006	24H008
24K008	24K009	24K013	24L006	24I005	24K005	24K007	24K008	24I003	24I004	24J002	24J004
24M009	24P001	24P002	24Y001	24K009	24K013	24L006	24M006	24K002	24K003	24K004	24K007
Reviews:				24K009	24K013	24L006	24M006	24K008	24K009	24K010	24K011
23H037	24E002	24G002	24O003	24M009	24P001	24P002	24Y001	24L003	24L004	24L005	24L006
24R001	24T003			Surface Studies:				24L007	24L008	24M002	24M003
Second Order Doppler Shift:				23S097	23Y024	24B013	24C005	24M004	24M005	24M006	24M007
23M059	24B014	24I005		24D008	24D011	24E001	24F002	24M009	24P002	24T003	24Y001
				24G003	24K005	24K009	24M009	24Z003	24Z004		
				24P001	24P002	24Z003					

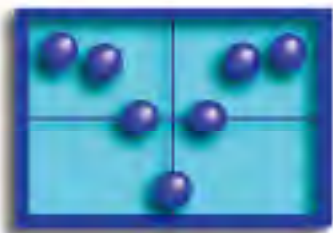
## ABBREVIATION LISTING

--	multiple components
IS/	isomer shift relative to
v	variable
xx	material not reported

## ISOTOPE INDEX

Eu-151:	24R001	24T003	
Sn-119:	24A011	24F001	24I005
Yb-171:	24O003		
Zn-67:	23M059		





# MÖSSBAUER SPECTROSCOPY NEWSLETTER

May 2024

## More Than 45 Years Worked in Mössbauer Spectroscopy

I am Bibicu Ion, Romanian citizen, born in a village in Braila County in December 1944. I went to secondary school and high school in Braila. In high school I liked exact sciences, primarily mathematics and physics. When choosing my profession I thought first of all about mathematics. I gave up on idea because I thought I wasn't talented enough to perform in mathematics. Following an idea from a mathematics magazine, I chose the profession of engineering physicist. Thus, in 1968 I graduated from the Department of Physical Engineers of the Faculty of Electronics and Telecommunications within the Polytechnic Institute of Bucharest. Based on my university results, I obtained an allocation at the Institute of Atomic Physics Bucharest-Magurele, one of the best in Romania.

In 1969, after completing my military service, I started my activity. I was co-opted in a team in formation that was mainly to deal with studies through Mössbauer Spectroscopy. The team was, at first, under the patronage of Academician Ioan Ursu and effectively led by Prof. Ph.D. Danila Barb. I obtained in 1981 the title of philosophical degree in physics with the thesis: *Mössbauer methods and Mössbauer spectrometers specialized for qualitative and quantitative determinations*, supervised by Prof. Ph.D. Danila Barb. The team had on average over time the following composition: 6 physicists, 1 chemist, 1 physical engineer (the undersigned) and 1 polyvalent technician. Among the physicists I note my colleagues: senior scientific researcher Ph.D. Lucian Diamandescu, prof. Ph.D. Mircea Rogalski. My fellow physicists were strong characters, but I managed to be in at least cordial relationships throughout my activity. I remained in the collective until my retirement: December 31, 2015. After the revolution of

1989 the Institute of Atomic Physics was divided mainly into 4 institutes and my team became part of the National Institute for Research and Development for Materials Physics. Currently, the collective no longer exists; its last members were integrated into another Mössbauer team in the institute led by senior scientific researcher Dr. Victor Kuncser.

My activity over the years has been carried out in the following directions: a) permanently ensuring the proper functioning of the installations; b) supporting an economic activity, complementary to the scientific activity of the collective; c) possibilities to extend and improve Mössbauer measurements; d) defining a personal research direction. In describing my work I will cite as few works as possible; those considered essential.



**Ph.D. Dipl. Eng. ION BIBICU**

### Permanent activity

Permanently ensuring the proper functioning of the equipments was at first a very stressful activity. I was inexperienced, I didn't have a colleague with whom I could advise and in addition I encountered problems that I had not heard about in college. I had to ensure all the conditions for the current activity of the installations (radioactive sources, consumables, installation upgrades, etc.) as well as the fastest possible commissioning

in case of malfunctions. Over the years, we have had Mössbauer spectrometers from the following companies: Elscint-Israel, Austin Associates-USA, Oxford Instruments-England, Science Engineering & Education Company-USA, Wissel-Germany.

### Economic activity

According to the legislation, until the 1990 revolution, research activity had to be accompanied by involvement in an economic activity. In this activity I was permanently involved, being an engineer. Thus, we coordinated the realization of 3 approved devices using the Mössbauer effect and a microproduction for 2 of them.

A portable analyser for rapid quantitative determination of cassiterite ( $\text{SnO}_2$ ), the main material in tin mineral industry, have been constructed as homologated prototype [1], [2]. The analyser is presented in figure 1 and it used the transmission geometry. Its electromechanical transducer (loud speaker type) was driven by a sinusoidal voltage with a frequency close to resonance frequency of the transducer. The quantities  $N_0$  (transducer at 0 velocity, resonance absorption) and  $N_\infty$  (out of resonance) were recorded in the same analysing time between 5 and 40 seconds. The quantity  $N_\infty$  was recorded only for the part of the sinusoidal voltage for which the off resonance condition was fulfilled. The principle scheme of the analyzer was the subject of a patent granted [3]. The tin oxide analyser consists of a measuring head and a control and registration electronics in a separate box. The measuring head is designed to permit a variable distance between the radioactive source and the detector. The weight of the analyser was about 9 kg with possibilities to be used in the geological study of the ground. The  $\text{SnO}_2$  concentration is obtained by using a calibration curve which was plotted by measuring the effect on the samples with a known  $\text{SnO}_2$  content. Were obtained calibration curves near sensibility limit, theoretical estimated. The performances of the analyser were: range of tin concentration in powdered sample 0,05% - 10%; weight of sample 1g; the error at the sensitivity limit was lower than 30% and decreases for the increased tin oxide content; required average time for one measurement: 10-15 minute.

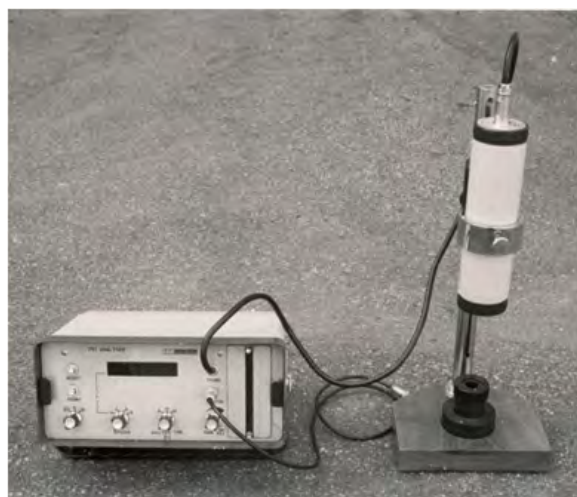


**Fig. 1.** The view of the analyser for quantitative determination of tin oxide ( $\text{SnO}_2$ )

A specialized Mössbauer spectrometer was developed for the rapid determination of iron and its compounds in mineral and rock samples (iron analyzer), as homologated prototype. The analyser, shown in figure 2, allows the qualitative and quantitative determination of up to 3 iron compounds (mainly oxides) in a sample or of total iron. The iron compounds under consideration are the main iron minerals: hematite ( $\text{Fe}_2\text{O}_3$ ), magnetite ( $\text{Fe}_3\text{O}_4$ ), siderite ( $\text{FeCO}_3$ ), goetite ( $\alpha\text{-FeOOH}$ ), ilmenite ( $\text{FeTiO}_3$ ), pyrite ( $\text{FeS}_2$ ). The compounds concentrations were obtained by using a calibration curve which was plotted by measuring the effect on the samples with a known compound content. The device can also be used as a Mössbauer spectrometer operating in constant speed mode. The device, designed for transmission geometry, worked at constant speed and was able to automatically explore any area of the Mössbauer spectrum. The designed analyzer combines the versatility of a laboratory Mössbauer spectrometer with the speed and simplicity of a specialized Mössbauer spectrometer. The construction of the analyzer and the related working methodology were the subject of a patent [4]. The analyzer is made in the form of 2 distinct subassemblies: NIM rack (frame) and optical bench stand.

The first 2 devices and the results obtained with them were capitalized through scientific research contracts, 1977-1979 period, on the topic "Development of techniques for the applications of Mössbauer spectroscopy in determining Sn and Fe from rock samples"; contracts financed by the Vienna Atomic

Energy Agency (IAEA). In the experimentation and valorization of the 2 devices, a general procedure for determining the background in Mössbauer effect measurements [5] was developed and the methodology for performing quantitative determinations of iron (oxides, siderite) and tin (casiterite) by Mössbauer spectroscopy was established.

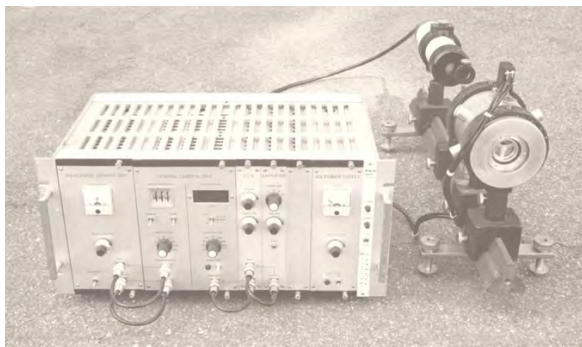


**Fig. 2.** The view of the iron analyser

The experience gained in the construction of previous devices resulted in the development of a universal Mössbauer spectrometer, an homologated prototype. Under the name of universal Mössbauer spectrometer, the essential part of such a device was realized: the system for achieving the relative source-sample motion and its associated electronics (function generator, electrodynamic vibrator control electronics, electrodynamic vibrator) [6]. The function generator provides a digitally obtained reference voltage. The device made in NIM system works in transmission geometry and in constant acceleration or constant velocity mode. At the time of its development, its linearity was superior to imported spectrometers and iron analyzers. The basic performances of the device are: working mode: constant velocity and constant acceleration; velocity range: 0-10cm/s; number of velocity steps: 256, 512; full linearity for speed range  $0-1\text{cm/s} \leq 0.5\%$

As project director I capitalized on the last 2 devices by carrying out a microproduction: microproduction of 5 iron analyzers during 1979-1984, the beneficiaries being the universities of Bucharest, Cluj and Brasov, the Institute of Geology and Geophysics-Bucharest and the Institute for Mining Research-Deva and a microproduction of 3 Mössbauer spectrometers between 1983

and 1995, the beneficiaries being: IRNE Pitești, University of Cluj-Napoca and IFIN Bucharest.

Also I participated at the studies of industrial Fe-C steels, [7] Fe-Si electrotechnical steels [8] and the compound formed at the Fe-Sn interface of a babbit bearing [9].

### **Extension of measurements by the Mössbauer effect**

Fellow physicists wanted additional information from the Mössbauer measurements. In order to obtain them, it was necessary to modify the conditions of their accomplishment, apart from the standard equipment offered by companies producing accessories for Mössbauer spectrometers. Thus, new experimental arrangements were made, to which I contributed. I will present below the most representative ones.

A transmission Mössbauer polarizer, which can be attached to any standard Mössbauer spectrometer was achieved [10]. It allows the use of the same transmission geometry for the Mössbauer spectrum and for the Malus curves corresponding to different energies of the polarized gamma ray. The experimental arrangement is shown in figure 3. The Malus curve provide information about the three polarization parameters: intensity, azimuth rotation and excentricity. The polarizer can be rotated uniformly by a syncromotor with a rotation period in the range of one sweep period for Mössbauer spectrum and the set-up worked as an “automatic polarimeter”

An improved equipment for continuous and pulsed radiofrequency (RF) Mössbauer experiments with an increased capacity to minimize the RF-heating effects was realised [11]. Was possible to obtain spectra in the presence or in the absence of a RF field for similar sample temperatures. The equipment was used successfully to study the influence of a magnetic radiofrequency (RF) field on the properties of ferromagnetic materials, to effect RF treatments on small samples. The equipment, designed as an additional part to an AME-50 Mössbauer spectrometer and a Promeda-01 programmable data acquisition and processing system, is schematically represented in figure 4. The interface circuit (IC) receives the start signals from a function generator (FG) and produces the enable signals for the linear gate circuit (G) and the new start



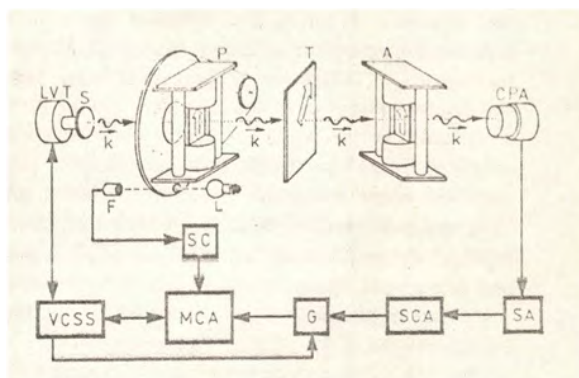


**Fig. 3.** Experimental arrangement for transmission Mössbauer polarizer

LVT: linear velocity transducer, VCSS: velocity control servo system, CPA: NaI(Tl) crystal photomultiplier assembly, SA: spectroscopy amplifier, SCA: single channel analyser, MCA: multichannel analyser multicanal, SC: synchronization circuit, G: gate circuit, S: radioactive source, P: gamma-ray polarizer, T: thick absorber, A: gamma-ray analyser, L: light source, F: phototransistor

signals for the data acquisition system (MCA). This circuit also routes the signals from a single channel analyser (SCA). By means of the gate circuit, the RF power provided by the radiofrequency oscillator (RFO) and amplified by the RF power amplifier (RFA) is applied continuously or switched to the absorber (A) placed inside the coil (L) of a resonant LC tank circuit. The LC-tank circuit enhances the field strength applied to the absorber and it is commonly used in nuclear magnetic resonance (NMR) studies. The resonant circuit is divided into two parts in order to separate physically the absorber from the rest of electronics. The first part, the matching assembly (MA) consists of two capacitors C and C/. The capacitor C together with inductance (L) forms the resonant tank. The capacitor C/ serves to match the impedance to the 50  $\Omega$  input cable. The second part of the resonant circuit consists of a coil in which the sample is placed. The coil L is such constructed that the attenuation of Mössbauer gamma radiation is minimised. The matching assembly and the coil are linked together by a co-axial cable, one half-wavelength long, designated in figure by  $\lambda/2$ . The temperature of the sample during exposure was measured with an infrared pyrometer. The power amplifier is able to amplify RF signals over the range of frequencies 1-100 Mhz up to a power level of 100 W. The quality factor (Q) of the resonant LC tank circuit at the

frequency 55 MHz is  $Q=60$ . The RF field in the coil is parallel to the absorber plane and a field intensity from 0 to 20 Oe. Interface circuit assures a variable time between the applications RF field on the absorber. It makes possible to record the Mössbauer spectrum in the presence of the RF field and the second one in the absence of the RF field.

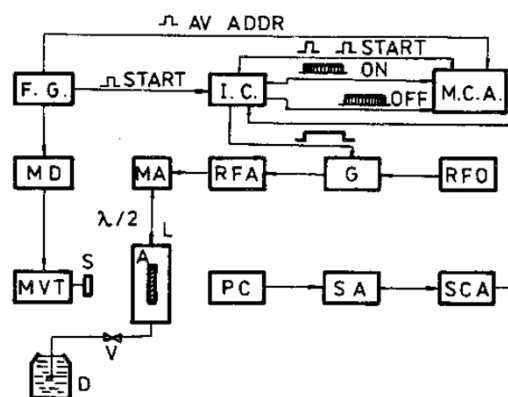


**Fig. 4.** The experimental set-up of the apparatus for continuous and switched RF Mössbauer experiments

A: sample; L: coil; MA: matching assembly; S: radioactive source; MVT: Mössbauer velocity transducer; MD: Mössbauer drive; FG: function generator; IC: interface circuit; G: gate circuit; RFO: radiofrequency generator; RFA: power amplifier; PC: proportional detector; SA: spectroscopy amplifier; SCA: single channel analyser; MCA: programmable data acquisition and processing system; D: nitrogen dewar flask; V: valve

The possibility of nuclear recoil compensation at the absorption of gamma-rays by means of optical photons was considered. The most convenient testing of the two-photon absorption mechanism would be within the frame of Mössbauer spectroscopy, due to the fact that the absorption cross-sections in this case are the highest. An experiment to check the cross-section for recoil-free gamma-ray absorption in the presence of a microwave field was achieved [12]. Schematic drawing of the experimental arrangement for the microwave-Mössbauer resonant absorption is shown in figure 5.

An experiment of recoil-free 14.4 KeV resonant gamma-ray absorption on polycrystalline  $K_3[Fe(C_2O_4)] \cdot 3H_2O$  sample exposed to a strong microwave field was carried out using a constant acceleration Mössbauer transmission spectrometer. The pulsed microwave field was generated by a magnetron (M) with the following characteristics: the power  $P = 1$  MW, the

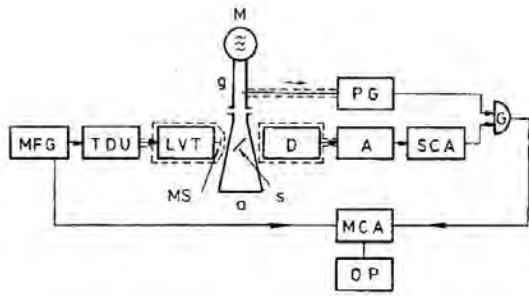


**Fig. 5.** Schematic drawing of the experimental arrangement for the microwave-Mössbauer resonant absorption

S: sample; MS: Mössbauer source; M: magnetron; MFG: Mössbauer function generator; TDU: transducer driving unit; LVT: linear velocity transducer; D: detector; A: spectroscopy amplifier; SCA: single channel analyzer; MCA: programmable data acquisition and processing system; PG: pulse generator; G: linear gate; g: wave guide; a: balanced resistive load; OP: data output/input device

frequency  $\gamma = 3$  GHz, the frequency stability  $\Delta\gamma = 50\text{KHz}/^\circ\text{C}$ , the pulse width  $\tau = 1\ \mu\text{s}$  and the pulse train frequency  $\gamma_r = 222\text{Hz}$ . The sample (S), originated from a single crystal as a finely ground powder, was uniformly pasted by silicon grease on a teflon support making a  $45^\circ$  angle toward the reciprocally perpendicular directions of the gamma-beam and the guided field propagation. Two reasons prevailed in the choice of the absorber: a) large enough linewidth to be detectable on the large Doppler velocity scale demanded by the experiment, b) absence of the internal or magnetic collective phenomena to avoid any acoustic or other undesirable RF effect. The electronics was carefully protected from the influence of the microwave field. A Doppler velocity scale of  $30\text{cm/s}$  was used to look for the first-order microwave sideband which was expected to appear at  $-25.8\text{ cm/s}$ . The perturbation observed in the spectrum obtained in this experiment can be attributed to a two-photon interaction

Due to the extraordinary high resolution of the Mössbauer effect, the Rayleigh scattering of the Mössbauer radiation can be used to separate elastically and inelastically scattered radiation from crystals not containing Mössbauer isotope. Also it permit to investigate lattice instabilities and structural phase transitions induced by the softening of an optical mode in solids. The relative complexity of the equipment required to perform Rayleigh scattering of Mössbauer is

a barrier to the routine use of this technique. These experiments are difficult essentially due to low brilliance of Mössbauer sources. The block diagram in figure 6 presents the final equipment. [13], [14]. There are very few such equipment in the world and for Romania was an opening. The set-up represented a long collaboration between our institute and Horia Hulubei National Institute for R&D in Physics si Nuclear Engineering. Our institute offered Mössbauer spectrometer and Mössbauer expertise.

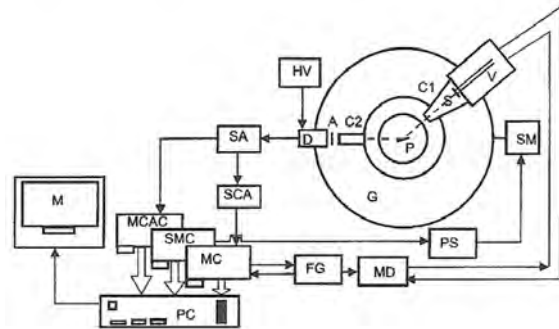


**Fig. 6.** Block diagram of the PC based set-up for Rayleigh scattering of Mössbauer radiation

G: goniometer; V: electromagnetic vibrator; S: Mössbauer source; P: scatterer; A: absorber; C1, C2 collimators; D: detector; HV: high voltage supply; SA: spectroscopy amplifier; SCA: single channel analyzer; SM: stepping motor; PS: power supply; FG: function generator; MD: Mössbauer drive; PC: personal computer; MCAC: multichannel analyzer card; SMC: stepping motor card; MC: card for acquisition Mössbauer data; M: monitor

The equipment for Rayleigh scattering of Mössbauer radiation is similar to a X-ray diffractometer with a Mössbauer source instead the X-ray tube. It consists of three main parts: a goniometer, a Mössbauer spectrometer and a personal computer. The goniometer (G), similar to those used in X-ray precision diffractometer, realizes the measuring geometry. On the goniometer are mounted the electromagnetic vibrator (V) with the Mössbauer source ((S), the scatterer probe (P), the nuclear resonance absorber (A), the detector (D). The Mössbauer source was  $26\text{mCi}$  of  $^{57}\text{Co}$  diffused into rhodium matrix. The incident and scattered beams are collimated by lead collimators ( $C_1$  and  $C_2$ ) with constant vertical divergence and variable horizontal divergences. For incident beam the horizontal divergence can be varied between  $0.5^\circ$  and  $2.8^\circ$  using different apertures. The absorber was an iron enriched  $^{57}\text{Fe}$  (30

atomic %) in a rhodium matrix: 12 microns thickness and 15 mm diameter. The sample and the source can be moved independently and in ( $\theta$ ,  $2\theta$ ) manner by a stepping motor (SM). A personal computer (PC) controls the orientation of the probe, the Doppler movement and realizes the acquisition of the amplitude spectra and Mössbauer spectra by means of three new cards: SMC, MC, MCAC. The performances of the system were tested using like scatters crystals with different mosaic divergences: lithium fluoride LiF(200) with 10' mosaic divergence and pyrolytic graphite C(002) with a higher divergence (up to  $1^\circ$ ). The equipment, suitable for any kind of Mössbauer scattering experiments, permits lower and adjustable horizontal divergences (from  $0.5^\circ$  to  $2.8^\circ$ ) of the incident beam and use of Mössbauer sources of lower intensity. The study on the pyrolytic graphite C(002) showed a smaller inelastic fraction than that reported for graphite and clearly evidence the contribution of coherent inelastic intensity to the total one. The normal-incommensurate phase transition in  $\text{RB}_2\text{ZnCl}_4$  was studied by Rayleigh scattering of Mössbauer radiation [15]. The discontinuity in resonance effect ( $\epsilon$ ) proved a stepwise variation of the inelastic component of the scattered radiation. The result was discussed in connection with photon-phonon interaction.

### Personal research direction

Over the years, as a result of collaborating with fellow physicists, I have considered it necessary and very useful to have my own research problem. The direction of research was suggested to me in the 1970s by a professor of physics from my faculty: Prof. G. Moisl. My research direction was surface studies by Mössbauer spectroscopy. First we developed detectors for surface studies and then we made various collaborations for Mössbauer surface measurements.

Were realized 4 proportional counters for conversion Mössbauer spectroscopy: detectors for conversion electron and transmission Mössbauer spectroscopy [16]-[18], toroidal detector for conversion X-ray and transmission Mössbauer spectroscopy (CXMS) [19], detector assembly for simultaneous conversion electron, conversion X-ray and transmission Mössbauer spectroscopy [17], versatile flow-gas proportional counter for electron detection

or X-ray detection function of geometry and gas [20].

All detectors are flow-gas type and operating at room temperature. Their construction permits for all detectors to realize simultaneous transmission and conversion measurements. The background due to photoelectrons is minimised by using low-Z materials as much as possible. The sample holder allows an easy manipulation of a sample, outside the detector and sample can always be repositioned in a reproducible manner with respect to the detector body. We have used for detectors an economical shielding which consists of a combination of lead, copper and steel disks. To destroy the characteristic radiation, alternate mounting of the lead, copper and steel disks were used. In order to absorb unfavourable KX-rays from the source, a plexiglas filter is placed in front of the shielding. We constructed flow-gas proportional counters for resonance electrons using two variants to dispose the anode wire: an exterior circle around the sample, and lines in front of the sample. The second variant has better performance. The test measurements argue the versatility of these counters for the comparative study of surface and bulk properties of Mössbauer samples.

The proportional detector for conversion X-ray and transmission Mössbauer spectroscopy [19] has toroidal shape of the space detection and a lower efficiency for the 14.4 keV  $\gamma$ -rays. The resonance effect can be optimised by a proper choice of the anode voltage and the filter. The design is simpler than those previously reported for similar devices.

The detector assembly [17] for simultaneous conversion electron, conversion X-ray and transmission Mössbauer spectroscopy consists mainly of two gas-flow proportional counters combined together and is represented in figure 7. The sample to be studied is mounted inside the smaller counter designed for detecting electrons backscattered from the sample. The larger counter is used to detect conversion x-rays that come from the sample and pass through the electron counter. This assembly has a low efficiency for backscattered 14.4 keV  $\gamma$ -rays. The counter design and operation are simpler than previously reported.



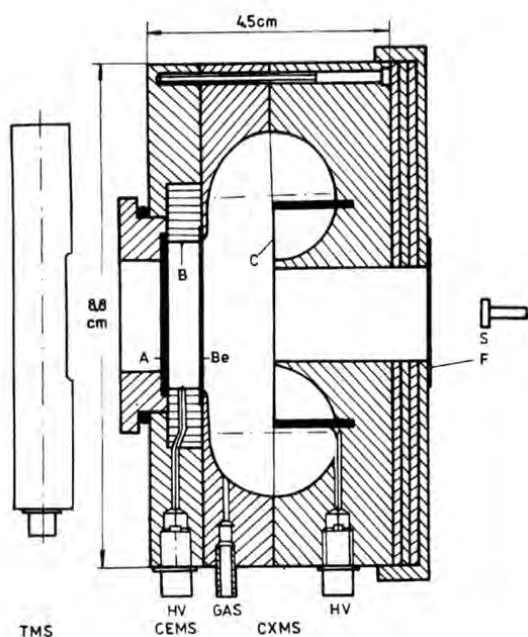


**Fig. 7.** The detector assembly for simultaneous conversion electron, conversion X-ray and transmission Mössbauer spectroscopy S: radioactive source; F: filter for X-ray; A: sample; Be: beryllium window; B: anodic wire for electrons; C: anodic wire for X-ray; HV: high voltage connectors; GAS: gas input/output; CEMS: electrons detector; CXMS: X-ray detector; TMS: gamma ray detector

The versatile flow-gas proportional counter for surface Mössbauer spectroscopy [20] represent a synthesis of my experience in the development of flow-gas proportional detectors for surface studies. The main improvements obtained by new design are: the height of the detection volume can be changed in large limits from 1 to 38 mm, the detection volume can be chosen symmetrical or not in respect with anode plan, the anode changing is easily and different anode configuration can be used. By changing the volume detection and flow gas it is possible to make measurements by electron, X-ray detection or gamma-ray detection. The diagram of this detector is present in figure 8.

I carried many studies by conversion electron Mössbauer spectroscopy (CEMS). So were investigated, for example: corrosion processes [21]-[29], the effects induced, mainly in surface, by pulsed radio frequency annealing of  $\text{Fe}_{81}\text{B}_{13.5}\text{Si}_{3.5}\text{C}_2$  (Metglass 2605 SC) glass [31]-[33], the structural and magnetic properties of different films:  $\text{Fe}_{81}\text{B}_{13.5}\text{Si}_{3.5}\text{C}_2$  films [34], Fe-ion-implanted Cu and Ag films [35], MnZnTi and NiZn ferrite films [36],

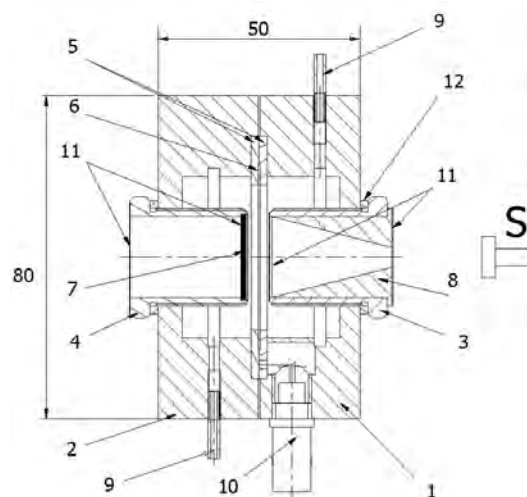


**Fig. 8.** The cross section of the versatile flow-gas proportional counter, 1 and 2 main parts of the counter, 3 input piece, 4 sample holder, 5 teflon insulator, 6 anodic ring, 7 sample, 8 collimator, 9 gas connection, 10 high voltage connector, 11 mylar windows, 12 tightness piece, S Mössbauer source

nanocrystallization process of the  $\text{Fe}_{87}\text{Zr}_6\text{B}_6\text{Cu}_1$  [37], investigation of electrolytic electroplating of Fe-C steel samples with low carbon content [38], superficial characterization of  $\alpha$ -iron oxides obtained by hydrothermal synthesis, the surface phase composition of bulk and thin films samples of  $\text{SnSe}^2$  and nanoparticle system  $\text{xSnO}_2-(1-x)(-\text{Fe}_2\text{O}_3)$ , surface measurements for samples containing  $^{151}\text{Eu}$  isotope [39], etc. The data obtained by these studies were correlated with those obtained by other methods.

### Final comments

Personally I am relatively satisfied with my work and am glad to have caught some of the peak period of the Mössbauer Spectroscopy.

I consider my best personal results to be: surface studies on samples containing the isotope  $^{151}\text{Eu}$  [39] and versatile flow-gas proportional detector for Mössbauer surface spectroscopy [20].

I believe that surface measurements through  $^{151}\text{Eu}$  are a world first, in my opinion, and the theoretical explanation of the presence of electrons is correct. The amplitude spectrum obtained with  $^{151}\text{Sm}$  source and  $\text{Eu}_2\text{O}_3$  sample inside, in a geometry like that used for  $^{57}\text{Fe}$  isotope is presented in figure 9. Figure 10 shows the two Mössbauer spectra: one obtained in the same geometry as given amplitude spectrum and other in transmission geometry for a  $\text{Eu}_2\text{O}_3$  sample with  $10 \text{ mg/cm}^2$  thickness.

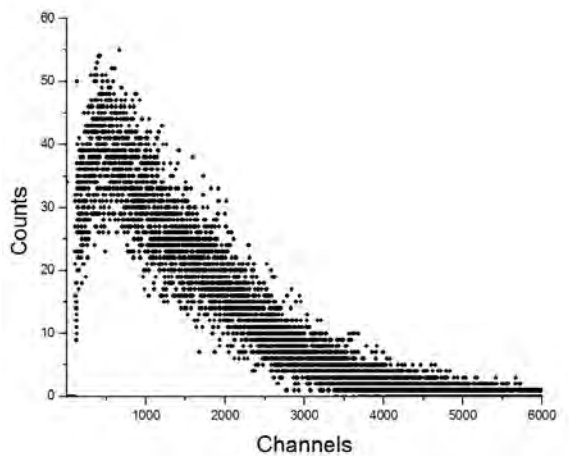


**Fig. 9.** Pulse height spectrum  $\text{Eu}_2\text{O}_3$  with  $^{151}\text{Sm}$  source, thickness of the detection volume: 4 mm.

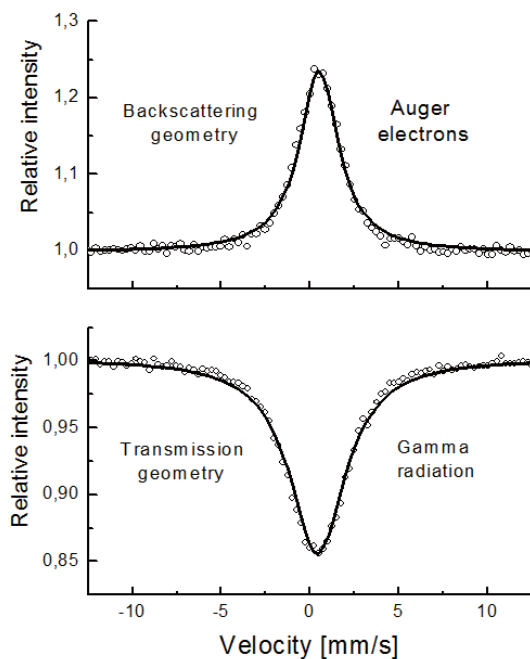


**Fig. 10.** Mössbauer spectra of  $\text{Eu}_2\text{O}_3$  obtained by Auger electrons (up) and transmitted gamma radiation (down);  $\circ$  data, — fit.

For the universal detector I like to present 2 spectra. According to my knowledge, the universal detector was the first time in the world to detect internal conversion X-rays (energy 3.44 – 4.13 keV) emitted by the radioactive source Mössbauer  $^{119\text{m}}\text{Sn}$  and obtain a surface Mössbauer spectrum by detecting them using a  $\beta$ -Sn sample, metal foil [17]. The Mössbauer spectrum is represented in figure 11. The spectrum shows the presence of a single line corresponding to  $\beta$ -Sn. The resonance effect,  $\varepsilon = 6\%$ , is smaller than that obtained by transmission geometry (7.9%) but the line width is smaller: 0.91 mm/s versus 0.98 mm/s.

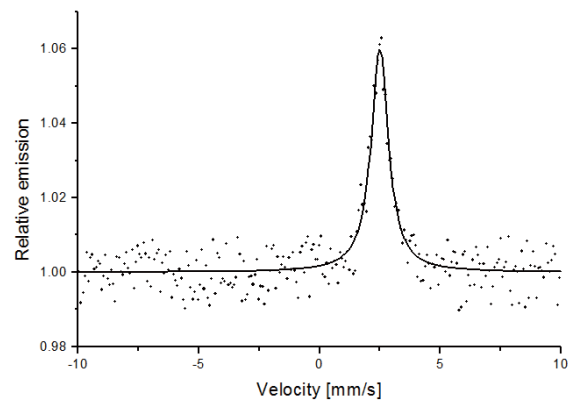


**Fig. 11.** Mössbauer surface spectrum of  $\beta$ -Sn obtained by conversion X-ray;  $\bullet$  data, — fit.

With versatile detector I obtained surface conversion X-ray spectra from the steel electrodeposited sample (thin Zn film of 8 microns at the surface of steel), for two velocity ranges [38], presented in figure 12. Spectra evidenced properly steel substratum and its parameters are practically the same as those obtained before deposition.

I personally regret that I did not succeed more in using Mössbauer Spectroscopy in economic activities. I think there were 2 reasons for failure: in a current use it does not allow obtaining quick results and the presence, the use of radioactive sources.

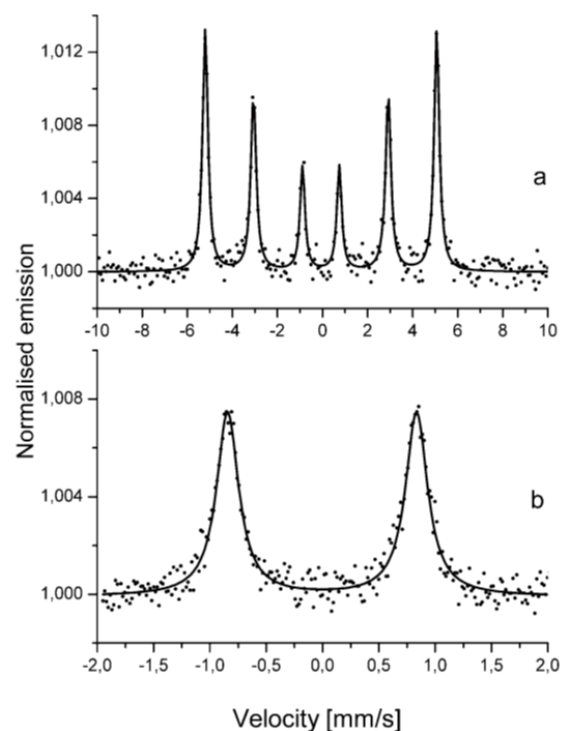


**Fig. 12.** Mössbauer spectra by CXMS of the steel Zn electrodeposited sample: a) at high velocity range; b) at low velocity range.

I believe that in recent decades Mössbauer spectroscopy has entered a relative decline evidenced by the difficulty of obtaining radioactive sources. For measurements on europium I used a radioactive source  $^{151}\text{Sm}$  with a half-life of 90 years bought in the mid-1970s. Back then there were 3 or 4 manufacturers of radioactive sources, now you can barely find one. The use of synchrotron radiation in obtaining Mössbauer spectra, in my opinion, is not a convenient solution for the vast majority of laboratories.

## References

- (1) Barb D., **Bibicu I.**, Prada B, *Analysers for quantitative determination of tin oxide ( $\text{SnO}_2$ ) by Mössbauer effect*, Rev. Roum. Phys., **22** (1977), p. 871-873.
- (2) Barb D., **Bibicu I.**, Voicu V., Prada B, *Determinarea cantitativa prin efect Mössbauer a bioxidului de staniu ( $\text{SnO}_2$ ) din roci, (Quantitative determination by Mössbauer effect of the tin dioxide from rocks)* St.Cerc.Fiz. **29** (1977), p. 637 – 642.
- (3) Barb D., Prada B, **Bibicu I.**, *Aparat pentru determinarea continutului de  $\text{SnO}_2$* , Brevet de inventie nr. 87846/30.09.1976 (*Device for determination of  $\text{SnO}_2$  content*, Invention patent no. 87846/30.09.1976)
- (4) Barb D., Balanescu M., **Bibicu I.**, *Procedeu si aparat pentru analiza rapida de faza a materialelor feroase*, Brevet de inventie nr. 76459/18.01.1981. (*Process and device for rapid phase analysis of ferrous materials*, Invention patent no. 76459/18.01.1981).
- (5) **Bibicu I.**, *A method for background determination*, Rom. J. Phys. **39** (1994) 1, p. 69-73.
- (6) Barb D., **I. Bibicu I.**, *Sistem de realizare a miscarii relative sursa absorbant pentru spectrometru Mössbauer*, (System to achieve relative motion source sample for a Mössbauer spectrometer), St.Cerc.Fiz. **41** (1989) 881-884.
- (7) Barb D., Morariu M., Tarina D., **Bibicu I.**, Constantinescu S., Diamandescu L., *Utilizarea efectului Mössbauer in studiul proprietatilor unor oteluri industriale Fe-C*, (The use of the Mössbauer effect in the properties study of some industrial steels), St. Cerc. Fiz., 25, 1973, p. 17- 26.
- (8) Barb D., Morariu M., Diamandescu L., **Bibicu I.**, *Internal magnetic fields in Fe-Si electrotechnical steels*, Rev. Roum. Phys., 19, 1974, p. 425-429.
- (9) **Bibicu I.**, Nat N., Barb D., *Study by Mössbauer Spectroscopy of the Fe-Sn interface from a babbitt bearing*, St. Cerc. Fiz., 41, 1989, p. 877 – 879.
- (10) Barb D., Rogalski M., **Bibicu I.**, *Transmission Mössbauer polarizer*, Nuclear Instruments and Methods **188** (1981) p. 469-471.
- (11) **Bibicu I.**, D. Barb D., *Improved equipment for continuous and switched RF Mössbauer experiments*, Meas. Sci. Technol., **7** (1996), p. 1793-1795.
- (12) Petrascu M, Barb D., **Bibicu I.**, Tarina D., *Recoil-free resonant gamma-ray absorption in  $^{57}\text{Fe}$  nuclei in the presence of a strong microwave field*, Hyperfine Interactions, **107** (1997), p. 247-255. (Gamma Ray Laser volume).
- (13) Enescu S. E., **Bibicu I.**, Zoran V., Kluger Al., Stoica A. D., Tripadus V., *A PC-based set-up for Rayleigh scattering of Mössbauer radiation*, Meas. Sci. Technology **9** (1998) p. 708-711.
- (14) Kluger A., Enescu S. E., **Bibicu I.**, Ciortea C., A. Enulescu A., *Mössbauer acquisition system for Rayleigh scattering experiments*, Rev. Sci. Instrum., **74** no.6 (2003), p. 3035-3038.
- (15) S.E. Enescu, **I. Bibicu**, M.N. Grecu, A. Kluger *Recoilless Rayleigh scattering on  $\text{Rb}_2\text{ZnCl}_4$  around the normal-incommensurate phase transition point*, Solid State Communications **111** (1999) No. 6, 299 - 303.
- (16) **Bibicu I.**, Rogalski M. S., Voiculescu Gh, Nicolescu G, Barb D., *Proportional counter for conversion and transmission Mössbauer spectroscopy*, Rev.Roum.Phys. **37** (1992), p. 315-317.
- (17) **Bibicu I.**, Rogalski M. S., Nicolescu G., *A detector assembly for simultaneous conversion electron, conversion X-ray and transmission Mössbauer spectroscopy*, Meas. Sci. Technol. **7** (1996), p. 113-115.
- (18) **Bibicu I.**, Rogalski M. S., Nicolescu G., *An improved proportional counter for conversion and transmission Mössbauer spectroscopy*, Rom. J. Phys. **45**, no. 1-2 (2000), p. 89-97.
- (19) **Bibicu I.**, Rogalski M. S., Nicolescu G., *Toroidal proportional detector for conversion X-ray and transmission Mössbauer spectroscopy*, Nuclear Instruments and Methods in Physics Research B **94** (1994), p. 330-332.
- (20) **Bibicu I.**, Nicolescu G., Cretu C., *A versatile gas-flow proportional counter for Mössbauer spectroscopy*, Hyperfine Interactions **192** (1) (2009) p. 85-91; DOI: 10.1007/s10751-009-9950-7.
- (21) **Bibicu I.**, A. Samide A., M. Preda M., *Steel corrosion in diluted ammoniac solutions studied by Mössbauer spectrometry*, Mat. Lett., **58** (2004), p. 2650-2653.
- (22) Samide A., **Bibicu I.**, Rogalski M., Preda M., *Surface study of the corrosion of carbon steel in solutions of ammonium salts using Mössbauer spectrometry*, J. Radioanal. Nucl. Chem., **261** (2004), p. 593-596.
- (23) Samide A., **Bibicu I.**, Rogalski M., Preda M., *A study of the corrosion inhibition of carbon-steel in dilluted ammonia media using 2-mercapto-benzothiazol (MBT) by Mössbauer spectrometry*, Acta Chim. Slovenica, **51** (2004), p. 127-136.
- (24) Samide A., **Bibicu I.**, Rogalski M., Preda M., *Surface study of the corrosion inhibition of carbon*

steel in diluted ammonia media using *N*-cyclohexylbenzothiazole-sulphenamida, *Corros. Sci.*, **47** (2005), p. 1119-1127.

(25) Patru Samide A., **Bibicu I.**, *Kinetics corrosion process of carbon steel in hydrochloric acid in absence and presence of 2-(cyclohexylaminomercapto) benzothiazole*, *Surface and Interface Analysis* **40** (5) (2008) p. 944-952,

(26) Patru A., **Bibicu I.**, Agiu M., Preda M., Tutunaru B., *Mössbauer Spectroscopy study on the corrosion inhibition of carbon steel in hydrochloric acid solution*, *Mater. Lett.*, **62** (2008), p. 320-322.

(27) Samide A., **Bibicu I.**, *Kinetics corrosion process of carbon steel in hydrochloric acid in absence and presence of 2- (cyclohexylaminomercapto) benzothiazole*, *Surf. Interface Anal.*, **40** (2008), p. 944-952.

(28) Samide A., **Bibicu I.**, Turcanu E., *Surface analysis of inhibitor films formed by *N*-(2hydroxybenzilidene) thiosemicarbazide on carbon steel in acidic media*, *Chem. Eng. Commun.*, **196** (2009), p. 1008-1017.

(29) Samide A., **Bibicu I.**, *A new inhibitor for corrosion of carbon steel in hydrochloric acid solution*, *Rev. Roum. Chem.*, **54** (1) (2009), p. 33-43.

(30) Rogalski M., **Bibicu I.**, *Surface short range order induced by RF annealing  $Fe_{81}B_{13.5}Si_{3.5}C_2$  glass*, *Mater. Lett.*, **13** (1992), p. 32-34.

(31) **Bibicu I.**, Rogalski M. S., Nicolescu G., *Transmission and conversion electron Mössbauer investigation of  $Fe_{81}B_{13.5}Si_{3.5}C_2$  glass under RF thermal treatment*, *Phys. Stat. Sol. (b)*, **178** (1993), p. 459-464.

(32) Rogalski M. S., **Bibicu I.**, Sorescu M., *CEMS investigations of surface hyperfine interactions in  $Fe_{81}B_{13.5}Si_{3.5}C_2$  glass*, *Hyperfine Interact.*, **92** (1994), p. 1317-1321.

(33) Rogalski M. S., **Bibicu I.**, *CEMS, CXMS and transmission Mössbauer investigation of the RF isochronal annealing of  $Fe_{81}B_{13.5}Si_{3.5}C_2$  glass*, *Physica Stat. Sol. (b)*, **195** (1996), p. 531-536.

(34) Rogalski M. S., Jackson T. J., **Bibicu I.**, Palmer S. B., *Deposition of  $Fe_{81}B_{13.5}Si_{3.5}C_2$  films by excimer laser ablation and their structural investigation*, *J. Phys. D Appl. Phys.*, **27** (1994), p. 2167-2170.

(35) Pereira de Azevedo M. M., Sousa J. B., Mendes J. A., Almeida B. G., Rogalski M. S., Pogorelov Yu. G., **Bibicu I.**, Redondo L. M., da Silva M. F., Jesus C. M., Marques J. G., Soares J. C., *Magnetization and magnetoresistance in Fe-ion-implanted Cu and Ag thin films*, *J. Magn. Magn. Mater.*, **173** (1997), p. 230-240.

(36) Amado M. M., Rogalski M. S., Guimaraes L., Sousa J. B., **Bibicu I.**, Welch R. G., Palmer S. B., *Magnetic properties of NiZn and MnZn ferrite films deposited by laser ablation*, *J. Appl. Phys.*, **83** (1998) p. 6852-6854.

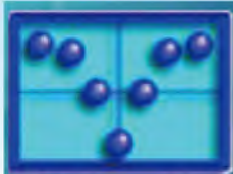
(37) **Bibicu I.**, Garitaonandia S., Plazaola

F., Apinanz E., *X-ray diffraction, transmission Mössbauer spectrometry a conversion electron Mössbauer spectroscopy studies of the  $Fe_{87}Zr_6B_6Cu_1$  nanocrystallization process*, *J. Non-Cryst. Solids*, **287** (2001), p. 277-281.

(38) **Bibicu I.**, Bulea C., Diamandescu L., Rus V., Popescu T., Mercioniu I., *Characterization of surface and interface of Fe-C steel under electrolytic galvanisation*, *Proceedings of the Romanian Academy - series A*, **19** (3) (2018), p. 423-430.

(39) **Bibicu I.**, *Some comments on  $^{151}\text{Eu}$  Surface Mössbauer Spectroscopy*, *Eur. Phys. J. Appl. Phys.*, **62** (1) (2013) 11302 (3 pages) Doi: <http://dx.doi.org/10.1051/epjap/2013120328>.





# Center for Advanced Mössbauer Spectroscopy

Dalian Institute of Chemical Physics, Chinese Academy of Sciences

is pleased to offer these services of the Mössbauer spectra (MS) measurement & analysis to the international community. Your any special request will be carefully considered.

## We offer

- ★ Room temperature  $^{57}\text{Fe}/^{119}\text{Sn}$  MS
- ★ Room temperature  $^{57}\text{Fe}/^{119}\text{Sn}$  CEMS
- ★ Low temperature transmission  $^{57}\text{Fe}$  MS
- ★ Frozen solution  $^{57}\text{Fe}$  MS
- ★ Electrochemical in-situ/operando  $^{57}\text{Fe}/^{119}\text{Sn}$  MS
- ★ Ion battery in-situ/operando  $^{57}\text{Fe}/^{119}\text{Sn}$  MS
- ★ Photocatalytic in-situ/operando  $^{119}\text{Sn}$  MS
- ★ Photoelectrocatalytic in-situ/operando  $^{57}\text{Fe}/^{119}\text{Sn}$  MS
- ★ Temperature, pressure and atmosphere control in-situ/operando  $^{57}\text{Fe}/^{119}\text{Sn}$  MS



## Contact

- ✉ Email: [mossbauer@dicp.ac.cn](mailto:mossbauer@dicp.ac.cn)
- ☎ Phone: +86-411-84379711
- 📍 Center for Advanced Mössbauer Spectroscopy  
Dalian Institute of Chemical Physics  
Chinese Academy of Sciences  
457 Zhongshan Road, Dalian 116023, China
- 🌐 <http://wangjh.dicp.ac.cn/csfw.htm>  
<http://wangjh.dicp.ac.cn/English/Services.htm>

**#Co-57**

**#Sn-119m**

**#Fe-57 reference absorbers**

**#Source grippers**



**Since 2023 → a new distributor in North and South America:  
ISOFLEX Radioactive LLC, [iso-rad.com](http://iso-rad.com), +1 (415) 440-4433**